Monte Carlo simulations of a small-animal PET scanner

Analysis of performances and comparison between camera designs

ANNA TURCO

Master's Thesis at KTH-STH
Supervisor: M Colarieti Tosti
Examiner: A Kerek

TRITA 2012:32

Abstract

The work here presented analyzes the performances (in terms of scatter fraction, spatial resolution, sensitivity, image quality) obtained from a 10-detectors small-animal PET, simulated via Geant4 Application for Emission Tomography (GATE), in comparison with other designs studied in previous works. Particular attention is given to the comparison with the 12-detectors miniPET II, already built and working, with the ultimate goal to understand if the removal of two detectors would substantially affect performances. Results obtained show a clear improvement in count rate and scatter fraction (-4% with respect to miniPET II and peak NECR of 114 kcps at 60 MBq with mouse phantom), as well as in sensitivity (maximum value obtained at the center of the camera with 10.91 cps/kBq); spatial resolution is as good as 1.58 mm FWHM in the transaxial plane, only 10% higher than miniPET II, and is confirmed by image quality tests on a mini Derenzo phantom. Results are encouraging and speak in favour of 10-detectors design.

Acknowledgements

Nobody walks alone in the journey of life. This project would not have been possible without the support, guidance and help of several people who, in one way or another, contributed to its completion. It is a pleasure to express my deep and sincere gratitude to at least a small part of them.

First of all, I truly want to thank my supervisor here in Sweden, prof. Massimiliano Colarieti Tosti: with his kindness and availability, he made me work with an incredible peace of mind. Being a great support and guidance, he always showed interest in what I was doing and faith in what I could do.
Thanks to my Italian supervisor, prof. Alfredo Ruggeri: for his unbelievable patience, for answering to all my questions and doubts with the fastest and clearest answers.
Thanks to Andras Kerek, for the time spent in reading, correcting and revising with me this report. To Wuvei Ren, for the same reason, and for being a great desk-neighbour.

Thanks to Anna and Clara, the best roommates I could have ever dreamt of. For sharing their thoughts with me, for being always lovely and patient even when I was nervous or sad. For listening to my never-ending school problems, showing interest even if I was explaining myself in the worst way ever.
Thanks to all of my university friends, but especially to Chiara, Elena, Serena and Martina, for the laughters we had together. For always believing in me and supporting me, even when I didn't deserve it, and even more when I was on the other side of the world. For having shared with me the burden of our worst exams, turning potential tears into unforgettable moments of fun.
Thanks to Sofia, beacuse I know she's always there, and to my high school teachers, prof.Strinati and prof.Bonaldo in primis, for being my second family.
Thanks to Elisa, without whose irony and 'take it easy' philosphy I wouldn't have survived Boston. Thanks to Durba, Ana-Claudia and Gene, for having shared never-ending reports and class hours. Thanks to the many, many happy and joyful guys I met in my semester in Sweden, on top of them to Laura, Dominik, Attilio, Sarah and Deborah. Thank you for the great, clean fun we had together. And for making this semester literally unforgettable.

Last but not least, many thanks to my family: without their support, I'd have never been where I am now; thank you, for having always struggled to give me the best. But particular thanks go to the most wonderful person in the world. For supporting me literally anywhere and at any time, for never leaving me alone; for believing in me, and for making me believe in me; for being my greatest, unconditionate fan and supporter. I will never stop saying you thanks, papa'.

Contents

Abbreviations

PET - Positron Emission Tomography
BGO - Bismuth Germanate (Bi4Ge3O12)
LOR - Line Of Response
DOI - Depth Of Interaction
PSF - Point Spread Function
FWHM- Full Width at Half Maximum
FWTM- Full Width at Tenth Maximum
FBP - Filtered Back Projection
MLEM - Maximum-Likelihood Expectation Maximization
OSEM - Ordered Subsets Expectation Maximization
SF - Scatter Fraction
NECR - Noise Equivalent Count Rate
NEMA - National Electrical Manufacturers Association
FOV - Field Of View

Chapter 1

Introduction

1.1 Small-animal PET

In the past few decades, the increasing need to image with more depth and precision small parts of the body or the physiological processes occurring in small animals have led to the development of the so called *small-animal PET cameras*. Those devices are able, for example, to image the smallest structures of breast or brain, or to portray with accuracy the physiological processes occurring in mice or rodents during tests of drugs or pharmaceuticals. For these reasons, the importance of small-animal PET cameras both in the research field and in medical practice is constantly increasing, helped by the recent progresses in computational capabilities, in electronics and in biology.
The design of small-animal PET devices, characterized by small Field Of View and very high spatial resolution, is however not free of obstacles: the small dimensions of the camera require a careful choice of the components used to build it up, in order to collect as much information as possible from those small emitting sources. At the same time errors, artifacts or distortions of the final image have to be avoided. The components of such sophisticated machines are far from cheap, so the development of a new camera has to be carefully thought beforehand. Virtual simulation of the device, performed before building up the actual machine, is one of the strategies used nowadays to optimize the process that leads to the development of a new small- animal PET scanner.

1.2 Project aims and objectives

The aim of this project is to analyze the performances of a 10-detectors PET scanner designed for small animals, using a Monte Carlo-based simulation software. The new geometry will be characterized in terms of sensitivity, scatter fraction, spatial resolution and image quality. The results will be compared with the ones obtained with the 12-detectors miniPET, simulated and later built in ATOMKI

laboratories, in order to obtain guidelines for a new small animal PET scanner that KTH and ATOMKI are planning to build. In fact, each detecting unit can greatly influence the costs of the final machine. As a consequence, finding a lower bound to the number of detectors that can guarantee good results at the same time is of outstanding importance.
These simulations will thus make evident either if removing 2 detectors from the previously evaluated miniPET II [1] is feasible (worth the reduced FOV and the possibly worse performances) or if the use of 12 detectors represents a lower bound to detector number, under which performances become unacceptable for a small-animal scanner.

1.3 Methodology and report outline

The tests listed in the previous sections are performed according to the recommendations of National Electrical Manufacturers Association, an organization that provides guidelines to test (not only medical) devices in a standardized and comparable way. The simulations are performed with a Monte Carlo based simulation software, specifically tailored to Tomographic applications (Geant4-based Application for Tomographic Emission, GATE). Matlab sofware package was used to process data coming from the simulations.

In chapter 2, an overview of PET imaging is presented, with particular attention to the aspects of interest for small-animal PET imaging. Chapter 3 briefly describes the basics of Monte Carlo simulations, together with the properties, advantages and disadvantages of the simulation software (GATE) used during this work. In Chapter 4, the implementative details of the 10-detectors PET here simulated are discussed, together with materials and methods used to characterize it. Discussion of the results obtained from the simulation are on Chapter 5. This chapter also includes the comparison with the miniPET II camera, evaluated in previous works, and with other (commercial and pre-clinical) devices of the same category.

Chapter 2

Nuclear medical devices: from radiotracers to image reconstruction

One of the first applications of nuclear imaging goes back to late 40s, when radioactive iodine was used for the first time as a means to diagnose thyroid cancer, using a point by point scan. From that first application, different devices have been designed in order to detect radiation emitted form the body: SPECT and PET are the main ones. In this chapter, a brief overview on the main principles underlying the proper working of these devices is presented; particular attention will be given to PET imaging.

2.1 Principles of molecular imaging

All emission imaging techniques require two main components to properly work: a radiopharmaceutical and a device that is able to detect the (radioactive) activity of that component. The radiopharmaceutical is a substance that is introduced in the patient's body through inhalation, swallowing or injection. It is made up of a molecule of interest for the body, combined with a radioactive isotope. The resulting component is attracted to specific organs, tissues or body areas; the camera detects the radiopharmaceutical presence and provides information about the functional processes that are taking place in that region. In this sense, the information that emission imaging can give to doctors and specialists differ from what x-rays, CT or MRI produce: while these techniques are "anatomical" —and thus just provide a (very good) morphological description of the area under analysis—, PET and SPECT techniques might determine the presence of a malignant spot based on functional biological activities.

2.2 Positron Emission Tomography (PET)

Positron emission tomography (PET) is one of the main applications of emission imaging. It is a tomographic technique that computes the three-dimensional distribution of radioactivity based on the annihilation photons that are emitted by positron emitter substances. Since the quantity of radiotracer introduced in the body is usually very low, PET allows to describe biochemical and functional processes by relatively safe and non-invasive means. The process by which PET works

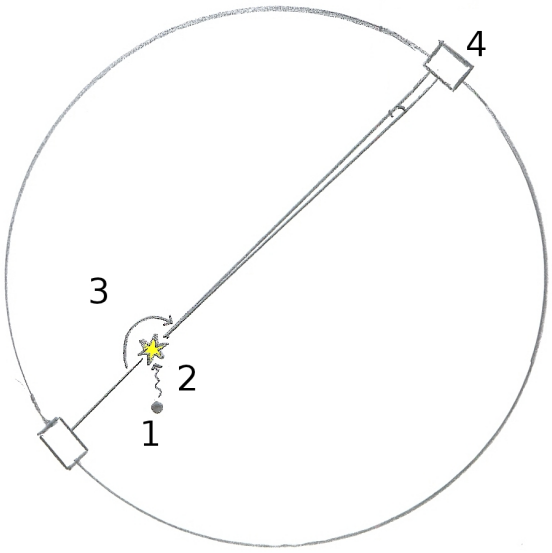

Figure 2.1: How PET works: 1) the radioactive molecule decays and a positron is emitted. 2) the positron travels some distance in the medium (see "positron range" further on), then annihilates. 3) annihilation at rest determines the production of two antiparallel gamma rays. In reality, the annihilation doesn't happen at rest ⇒ the two photons aren't emitted at exactly 180°angular span ("acollinearity angle") 4) each photon hits a crystal. If two photons are detected in the same coincidence window, a LOR between impinged detectors is identified. Given a sufficient number of LORs, reconstruction is made possible.

can be summarized in the following steps: first of all, the radioactive atoms contained in the radiotracer introduced in the body decay, emitting a positron and a neutrino:

$$A_Z \rightarrow A_{Z-1} + n + e^+ + energy \tag{2.1}$$

The positron (e^+) produced by this reaction travels in the medium (organ, tissue, phantom under examination) and, after a time approximately equal to 10^{-9} s, encounters an electron and annihilates. The annihilation determines the emission of

two gamma rays: they are antiparallel (emitted at 180°angular span, if annihilation is at rest) and they have an energy of E=511 keV, equal to the mass of the electron and/or the positron. These rays are emitted simultaneously and should be detected by the PET scanner.

The PET scanner is traditionally made up of a ring of detectors surrounding the object; the PET device should detect all photons emitted by the source, but only those pairs which hit two different detectors in the same (very short, i.e. 3 ns) temporal window will be considered as "coincidences" and will be stored for image reconstruction: in fact, if the two photons (having 511 keV energy) hit two scintillators almost simultaneously, this means that the annihilation site lies somewhere along the line connecting the two crystals (LOR, Line of Response). If this is done for a sufficient number of coincident events, it will be possible to reconstruct the distribution of the tracer within the FOV. Figure 2.1 sketches the main steps that lead from the decay of the molecule of interest to the detection of the respective Line of Response.

Types of coincidences

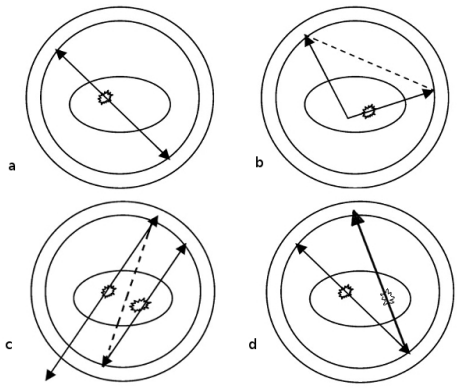

Figure 2.2: Coincidence events in PET: a) True b) Compton scatter c) Random d) Multiple. Solid line: photon path; dashed line: reconstructed LOR. Modified from [2]

The ideal process described in Section 2.2 would allow us to perfectly reconstruct a radioactive point source positioned in the FOV of the camera. However, in reality, other processes can occur in the meanwhile or after annihilation: the PET device will then also register falsely located coincidence events and, in turn, image resolution will be degraded. In the following part of this section, a brief explanation on the different events which can be recorded in PET imaging is given:

- A **true** coincidence is found when the two singles that make up the coincident event come from the same annihilation event.
  Scatter coincidences are true coincidences in which one of the two photons (or both) interacts with the body/phantom before reaching the detector; this means that the photon gets deviated with lower energy (Compton scattering) and hits a detector different from the one it was supposed to; by consequence, a wrong LOR will be reconstructed (Figure 2.2 , b).

It has to be noted that this definition of true coincidences (which includes scatter events) is often disregarded in everyday speaking. Almost always, true coincidences are considered as events that occur *when both photons from an annihilation event are detected by detectors in coincidence,* ***neither photon undergoes any form of interaction prior to detection*** [3]. This distinction between true and scatter coincidences is actually adopted by many sources of literature [2, 4]; the National Electrical Manufacturers Association [5] also suggests the calculation of 'true coincidences' as

$$C_{true} = C_{total} - C_{random+scatter}$$

which implicitly assumes that true and scatter coincidences are considered as two different types of event. Figure 2.2 also refers to this "alternative", but more common, way to address trues and scatters.

- **Random** coincidences are detected when two photons, coming from two different annihilation events, hit two detectors in the same coincidence window; again, a wrong LOR will be reconstructed (Figure 2.2, c)

- **Multiple** coincidence events (Figure 2.2, d) occur when more than two photons interact with detectors in the same coincidence window. In this case, the choice of which event is stored and which one is rejected depends on the camera (i.e., it is possible to reject all the events, to keep only the two photons with highest energy, ..., based on photon energy detection and gating).

It is important to understand the weight of all these components with respect to the total amount of coincidences detected. In fact, they can add background noise, decrease SNR and thus affect the quality of the reconstructed image.

Fundamental limits of spatial resolution in PET

Spatial resolution is a parameter of great importance, especially if small-animal PET cameras are considered. It is defined as the ability to distinguish between two points after image reconstruction and it is commonly measured by evaluating the Point Spread Function (PSF) of the reconstructed source.
Apart from spurious coincidence events, for which corrections can be applied, several other physical effects control the actual spatial resolution of a PET camera. The

literature [6, 7] shows that contributions can come from detector width, acollinearity of gamma rays and positron range, but also from inaccurate electronic decoding of signals, penetration of gamma rays into adjacent detectors and reconstruction errors. Some of these processes can not be avoided, while it is possible to get around some others by carefully designing the PET device.

Physical limits: acollinearity and positron range

Acollinearity represents one of the main fundamental limits in PET imaging resolution: since, after annihilation, the positron-electron pair still has some kinetic energy left, in order to preserve momentum the rays are not emitted at exactly 180°angular span; to be detailed, the mean accollinearity angle is 0.25°FWHM. The contribution of accollinearity of the two opposing rays increases with the ring diameter, so this problem is almost negligible when talking about small-animal cameras.

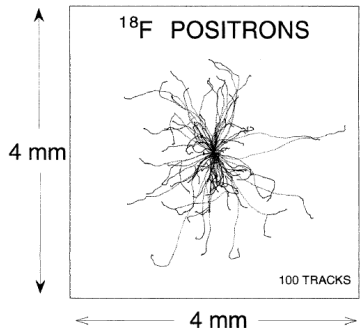

Figure 2.3: Positron range for a ^{18}F point source in water. [7]

The second main factor that limits PET resolution is the so called ***positron range***. Before colliding with an electron and going through the process of annihilation, the positron emitted by the nucleus of the radiotracer travels some distance in the material. This means that there is a discrepancy between the annihilation point (reconstructed with LOR) and the actual placement of the nucleus that generated the photon. The distribution of the actual annihilation points around the parent nucleus has a cusp-like shape and its FWHM only depends on the isotope being used; ^{18}F is one of the best choices since, with its 1.4 mm FWHM, is one of the isotopes with the lowest positron range [8].
A formula to analitically calculate spatial resolution G of a point source located at radius r from the center of the camera was derived some decades ago:

$$G = 1.25 * \sqrt{(0.0044 \times R)^2 + (\frac{d}{2})^2 + s^2 + b^2 + \frac{(12.5r)^2}{r^2 + R^2}}$$

where d is the crystal width, s is the positron range, b is the crystal decoding error factor ($d/3$ if optical decoding is used, 0 otherwise) and R is the ring radius. The factor 1.25 represents the contribution of interpolation and back-projection in the image reconstruction, and $0.0044 = tan(0.251)$ (more details can be found on [7]).

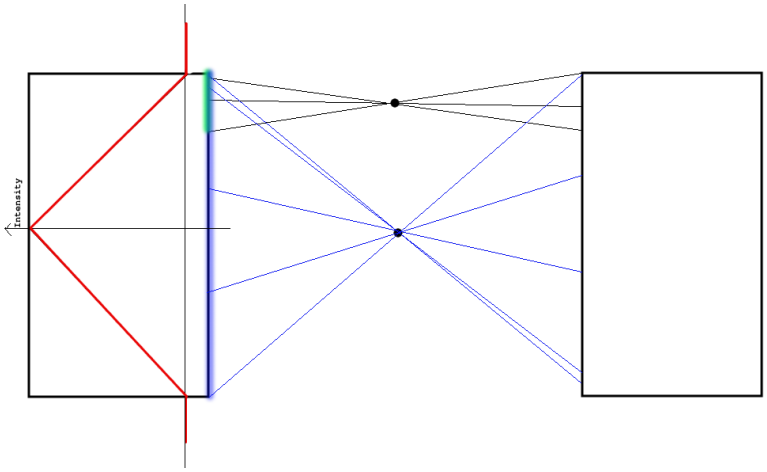

Figure 2.4: Detection response as a function of source position and crystal size: if the source is located at the edges of the FOV of the crystal, only coincidences from a restricted area (painted in green) can be recorded, while all other events are lost. If the same source is positioned at the center of the FOV, coincidences coming from a larger area (blue) can be stored. Using two small crystals, instead of a big one, would have allowed the collection of a higher number of coincidences even for the off-centered source.

Let's consider only the effects of positron range and acollinearity, reduce any other factor to ideal levels and assume the use of ^{18}F isotope. The **fundamental limit** of spatial resolution of a point source located at the center of a a small-animal ring PET scanner with R=77 mm (like the one simulated in this work) then becomes:

$$1.25 * \sqrt{(0.0044 * 77)^2 + (0.55)^2} = 0.81 \text{ mm FWHM}$$

.

Technological limit: crystal size

The **size of the crystals** that make up the PET device is another factor that can play and important role in determining spatial resolution. It has been demonstrated [6] that the detection of photons is not uniform at every point of the detector, but it goes from zero when the source is out of the edges of the detector to a maximum when the source is halfway between the edges, leading to a triangle-like response of the detection function (Figure 2.4). The triangle-like response of the detection function would ideally suggest the production of smaller crystals but, on the other hand, reducing their size would increase the number of crystals needed (and so the number of electronic channels needed, and therefore the costs); moreover, the

smaller the crystal, the higher the fraction of its volume occupied by the crystal coating, and this would lead to a reduction of its detection efficiency. Finally, for cameras whose diameter is smaller than 20 cm, significant improvements in spatial resolution would only be achieved if the crystal size is <1mm [7].
All of this to say that detector size is important, but not crucial in spatial resolution evaluation, and that its choice is the result of a compromise between costs, efficiency and spatial resolution ability.
Introducing now a realistic crystal width, the formula used in the previous paragraph to calculate the minimum spatial resolution of a small-animal PET scanner (assuming a point source, crystals with Depth Of Interaction capability –see further on on this paragraph for an explanation of DOI problem– and no decoding errors) becomes

$$1.25 * \sqrt{(0.0044 * 77)^2 + (0.55)^2 + (1.27/2)^2} = 1.14 \text{ mm FWHM}$$

This calculation was done by using 1,27 mm-wide detectors, the same used for the simulation presented in this work. This value was chosen for comparative purposes (miniPET II was built up with crystals of the same size), but it also makes sense since crystal width should be higher than the fundamental limit, but not too big —in order to reduce the artifacts due to the non-uniform detection of LOR, as said before.

Talking about crystal dimensions, one more point regarding crystal thickness has to be highlighted. The finite thickness of the crystal and the penetrating nature of photons, together with the fact that the electronics of the detectors is only able to calculate an integrated signal at the end of the crystal, determines a Depth of Interaction (DOI) uncertainty(Figure 2.5). The resulting *parallax error* determines the reconstruction of a wrong LOR, which in turn degrades the quality of the reconstructed image.

The factors just listed are those that most affect spatial reslution: for some of them (acollinearity and positron range) no realistic workarounds have been found yet. For some others (e.g. crystal front size) the choice is a trade-off between opposing needs. All the other factors listed before (reconstruction algorithm, imprecise electronics, ...) are potential sources of errors aswell, but they can be ideally avoided by e.g. designing crystals that are able to give information about the depth of interaction within the crystal or evaluating more sophisticated reconstruction algorithms.
For a detailed description of all these factors, refer to [7] and [6].

PET detectors

In Section 2.2 a mention to scintillating *crystals* was made, using this word to address the smallest detection element of a PET device. In this work we usually refer to *crystals* as submodules of a larger structure called *detector* (i.e., a detector is an array of crystals) but, literally speaking, crystals are **radiation detectors**, that is structures able to detect the amount of radiation emitted by the source.

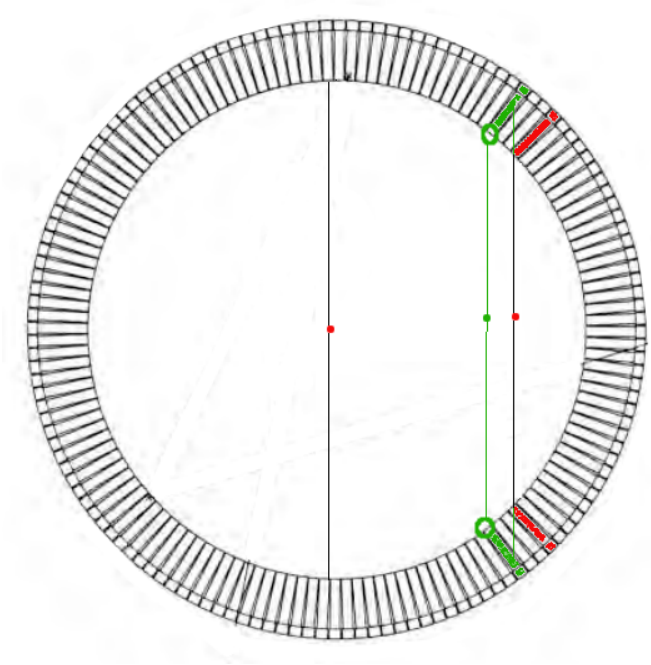

Figure 2.5: Parallax effect due to DOI uncertainty. It could happen that the detector's electronics could (incorrectly) assign the LOR based on the front of the interaction crystal (painted in green), that may not be the same as the one in which the ray entered (painted in red)

In order to work properly, they require interaction of radiation with matter; this interaction can be achieved either by ionization (removal of electrons from the atoms constituting the detector) or by excitation (elevation of electrons to excited states and subsequent decay with light emission).
Generally speaking, there are several ways to manufacture radiation detectors:

- *gas-filled* detectors consist of a volume of gas between two electrodes, with an electric potential difference applied between the electrodes. When a charged particle enters the chamber, it ionizes the gas and an electrical current is produced. The sensitivity of ion chambers can be increased by filling them with a high atomic number gas and by pressurizing the gas itself to increase its density. The main disadvantage of this kind of crystals is that they have low efficiency for γ rays and it is harder to pack them into tight arrays.

- ***scintillators*** are materials that emit visible or ultraviolet light after interaction of ionizing radiation with the material. The luminescence that is produced comes both from fluorescence and phosphorescence: fluorescence is the

prompt emission of light, while phosphorescence (or afterglow) is the delayed emission of light; ideally, afterglow should be as low as possible. They are able to measure the energy of the detected photons and they are those that are most widely used in PET scanners, due to simplicity, relatively low manufacturing costs and possibility to decrease their size down to less than 1mm [9].

- *semiconductor* detectors (or Solid-State Detectors, SSD) are essentially the solid-state version of gas-filled detectors, with the advantage that less energy (10 times lower [10]) is required in SSDs to create an electron-ion pair. Semiconductor detectors are seldom used in medical imaging mainly because of high expense and low intrinsic efficiency. However, this type of detectors could be the best way to achieve high signal output with short decay times and good linearity of response [11].

When a radiation detector is coupled with electronic circuitry, we can talk about a **detector system**. A detector system can work in two modes: *pulse mode* and *current mode*. In pulse mode, signals from each interaction are processed individually; the main disadvantage of this type of working modality is that two interactions must be separated by a finite amount of time if they are meant to produce two different signals. If the second interaction occurs during this time interval, there could be dead-time information loss or, even worse, it may even distort the signal from the first interaction. See Section 5.1 on Chapter 5 to have an idea on how much deadtime can impact on performances of a PET device.
In current mode, signals from several interactions are averaged together to produce a net current. This working modality is not affected by dead time information loss, but we lose information on individual interactions.
Scintillation detectors are obtained by optically coupling a scintillator with a device that converts light into an electrical signal (e.g. a photomultiplier tube, PMT): ionizing radiations fall on a scintillator, that in turn emits visible or UV light according to its light yield; a fraction of the light emitted by the scintillator is collected by the photosensitive cathode of a photomultiplier tube. The photoelectrons emitted by the cathode are amplified manyfold by the PMT giving rise to a large current pulse. With or without further electronic amplification, the output pulses are then counted or analyzed (pulse height, pulse time characteristics,..).

There are some properties that have to be taken into consideration in choosing the right radiation detector for each application: these are efficiency, cost, physical form, chemical stability and mechanical strength. Moreover, there are some other parameters that are especially important in choosing the scintillator: output wavelength, light yield, proportionality and decay time. The following of this section will briefly describe the most important of all these properties; for more details, refer to [12] and [11].

- Detection efficiency (or sensitivity, E) is the ability of a detector to detect radiation.

$$E = G * I$$

  where G is geometric efficiency, given by the ratio between the number of photons reaching the detector and the number of photons emitted by the source. I is intrinsic efficiency (or Quantum Detection Efficiency, QDE), given by the ratio between the number of photons detected and the number of photons reaching the detector; it depends on the energy of photons, on atomic number, density and thickness of the detector. For a detector of uniform thickness x, $I = 1 - e^{-\mu x}$, where μ is the linear attenuation coefficient of the material.

- Light yield (or light gain, or conversion efficiency): it is the number of photons emitted per unit of energy; is it usually measured as photons/eV. The higher the light yield, the better the accuracy, the spatial resolution and the energy resolution of the detection device.

- Decay time and afterglow: the decay time of a scintillator is defined by the time after which the intensity of the light pulse has returned to 1/e of its maximum value, while afterglow is the fraction of scintillation light still present for a certain time after the X-ray excitation stops [3]. Decay time should be as short as possible, in order to enhance timing resolution (especially in pulse-mode detectors used in coincidence), to allow high counting rates and Time-of-Flight modes.

- Cost, usually referred to as the cost of growing the crystal. In fact, the cost of crystal growth and manufacturing (cutting, polishing, assembling, ...) is usually much higher than the cost of the raw materials.

- Mechanical strength and physical properties: crystals have to be resistant not only to humidity, temperature changes and time, but also to the many phases of manufacturing they have to go through. Moreover, they have to possess the correct ruggedness in their surface and to minimize light reflection. Their coating doesn't have to be too thick with respect to the total volume (otherwise, scintillation volume will decrease) and their shape can be modified in order to achieve better results in detection efficiency and resolution (e.g. wedge-shaped scintillators).

Ideally, a good scintillator should have high light output, short decay times and linearity of response, that is to say it has to be both bright, efficient and fast. PET detectors have to work at high count-rates, so it is important that the decay time of the scintillator stays short. Moreover, secondary scintillation and afterglow should be low, because they can contribute with background light. For a long time, the scintillator of choice for PET cameras using block-detectors has been Bismuth Germanate (BGO), which has a high effective atomic number, is humidity-resistant

and does not suffer from secondary scintillation components. However, it has a low light yield and a long response time, so there is much interest in introducing new scintillator materials, even at the cost of lower intrinsic efficiency.

LSO/LYSO and LuAP/LuYAP are very interesting candidates to replace BGO in PET. Even if the probability of photoelectric effect is smaller, they have attenuation lengths that are comparable to that of BGO, a higher light yield and a much faster response [10]. Various studies are going on to determine which material is most suitable for PET applications. An interesting comparison, which especially addresses to small-animal PET cameras, is on [13]: although not free from disadvantages, LYSO crystals look very promising among scintillation detectors.

PET tracers

The radiopharmaceuticals used in PET imaging can affect, even minimally, the quality of the images obtained. All the molecules used in nuclear medicine have to satisfy some minimal requirements: they don't have to be toxic for the patient and they don't have to modify the biological processes under examination; they should be as specfic as possible for the process under study (they don't have to join other molecules or follow ways other than the one expected). In addition, they should show high affinity for the target site, in order to generate images with good contrast and low background noise. Finally, among all other properties, the molecule has to be easy to synthetize and must have a kinetics and decay time that is compatible with clinical needs. Too short decay times make it impossible to acquire a sufficient number of coincidences, while a too long half-life wouldn't be practical in routine clinical exams. The first and most commonly used tracer is the glucose analogue ^{18}F-FDG (also referred to as ^{18}F or FDG), obtained by substituting an atom of unstable ^{18}F to the hydroxyl group in the 2nd position in the glucose molecule. Since it was demonstrated that FDG accumulation in tissue is proportional to the amount of glucose utilization, this molecule has become widespread in everyday clincal practice. In fact, it is relatively easy to produce, its decay time is ideal in everyday medical practice (110 min) and, importantly, it is able to pass through the blood-brain barrier. The increased glycolytic rate and glucose avidity of malignant cells in comparison to normal tissue is the basis of the importance of FDG-PET in medicine studies.
However, ^{18}F-FDG is not free from disadvantages, first of which the fact that the increased glucose uptake is not specific for tumors: inflammed lymphnodes or normal processes in hyperglycaemic people could require an amount of glucose higher than the normal amount, thus possibly leading to wrong interpretations of PET output.
Several new PET tracers have thus started to be developed, with the main objective to target processes that are different from glycolysis, and possibly more specific. For example, in relation to breast cancer, ideas go towards targeting DNA replica-

tion or estrogen or epidermial growth factor receptors, whose altered activity could be sign of abnormal cell proliferation [14]. To detect Parkinson disease, which is caused —among all— by insufficient production of dopamine in certain nervous areas, it was thought to label the membrane D1 transporter or the protein aggregates which are typical of neurodegenerative disorders [15]. Many other studies are under development.
The two radiotracers used in this work are some of the simplest radioactive molecules and they are recommended by NEMA [5]. One is the already cited ^{18}F-FDG, which is good to simulate a realistic activity within a phantom. The second is ^{22}Na. The latter has a considerably long half-life (2.602 years) and this fact guarantees stability throughout the time of measurement. By consequence, it is the molecule of election to generate radioactive point sources and evaluate spatial resolution and sensitivity of PET devices.

2.3 Image reconstruction algorithms

The only information that comes from Positron Emission Tomography tests are the Lines of Response accounting for each annihilation event. If LORs all lie in the same transaxial plane (this is the case of a single-ring camera — see further on to see what happens if the camera has an axial extent), the most common and simple way to use them is to organize them into a *sinogram*, which is simply an ordered way to store LORs into sets of parallel projections. Later, the sinogram has to be reconstructed in order to get an image describing the distribution of the tracer within the object.

From list-mode data to sinogram

In this work, LORs are obtained from the simulation software output. They are subsequently translated into the corresponding sinogram using a Matlab program specifically written. In a few words, this is how the algorithm works (see Figure 2.6):

1. an empty matrix, which will contain the projections of the tracer distribution at the different projection angles (sinogram), is created

2. each LOR is defined by the (x, y) coordinates of the two impinged crystals. For simplicity, all LOR are oriented so that the angle they form with x axis is $0 \preceq \alpha \preceq \pi$.

3. the distance (d) of each LOR from the center of the camera is calculated (point-to line distance)

4. In order to establish if the LOR falls before or after the midpoint of the projection histogram, the angle (β) formed by the line that connects the first

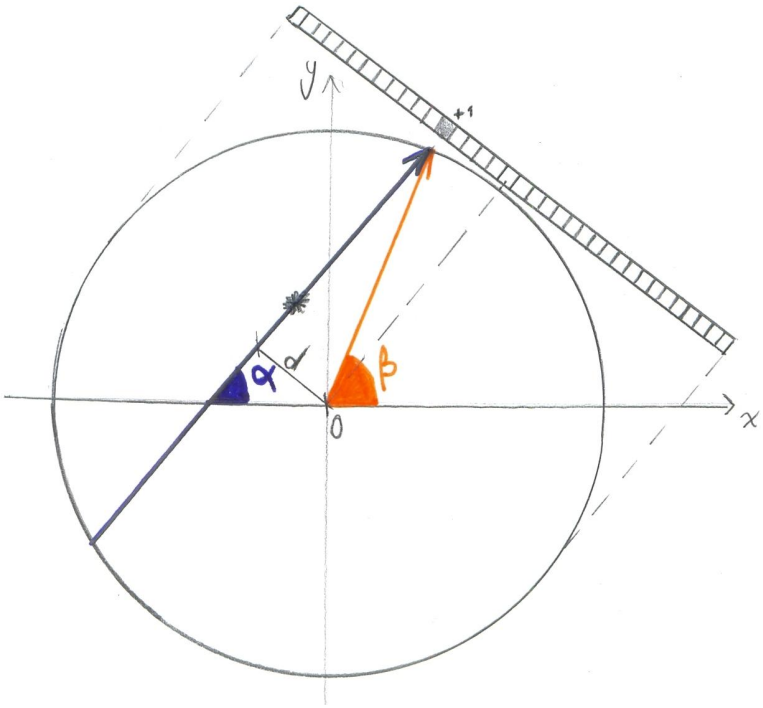

Figure 2.6: Sketch of geometry used for sinogram reconstruction. Blue line: LOR (always oriented upwards). Orange line: vector that connects center of camera with 1^{st} crystal. d= center-to-LOR distance.

crystal and the center of the camera is evaluated: if $cos(\alpha) > cos(\beta)$, the LOR falls before the midpoint (and so d=-d). Otherwise, d keeps its sign.

5. the intensity of the bin of the projection column with distance d from the midpoint is increased by one unit

6. the process is repeated for each LOR

2D sinogram backprojection

The sinogram now contains in each of its columns an intensity profile obtained at a particular projection angle. This information is very useful but not at a glance: in order to extract from the sinogram an image that depicts the actual distribution of the tracer within the scanned FOV, the sinogram has to be *reconstructed*. The reconstruction algorithms that have been developed throughout the years are numerous: simple backprojection of the intensity profiles onto the considered plane was the first attempt, soon extended and improved by Filtered back Projection

(FBP), whose mathematical basis lies on Fourier Slice Theorem. Another group of effective algorithms makes use of statistical, iterative techniques(i.e. ML-EM, Maximum Likelihood-Expectation Maximization; OS-EM, Ordered Subsets-Expectation Maxiamization; ...).

(Filtered) backprojection

The first, straightforward method used to reconstruct an image from intensity profiles stored in the sinogram was simple backprojection: considering each intensity profile, the value of each point in the projection profile is added down to every point in the corresponding image space. This is done for each intensity profile stored in a sinogram, eventually reconstructing the image. Simple backprojection is mathematically supported by Fourier Slice Theorem [16] [3]. Briefly speaking, this theorem states that the 1D-Fourier Transform of the intensity profile taken at a certain projection angle corresponds to the 2D-Fourier transform of the imaged object, evaluated on the radial line from which the projection was taken. This means that, calculating 1D-FT of each intensity profile and then anti-2DFT it, and repeating the process for each projection angle, it is possible to extract the image again. The result of this process is, actually, a heavily blurred version of the original image. The mathematical interpretation of backprojection, however, comes to help: if the image is blurred, multiplying the 1D-FT of the intensity profile by a ramp filter which emphasizes edges and de-emphasizes low-frequency content is the first, immediate choice; this would work perfectly if data were free from noise, but this is practically impossible in true acquisitions. The main consequence of ramp-filter multiplication is then not only to reduce blurring, but also to increase the contributions of high-frequencies (noise included). To reduce this effect, variants of the ramp filter have been studied, which try to remove blurring while keeping low the noise in the image.
To now, FBP is one of the most used reconstruction algorithms, due to its simplicity and to the fact that it is computationally fast. Its algorithm is implemented by many software packages, among which Matlab, and its use is recommended by National Electrical Manufacturers Association (NEMA).

Iterative methods

Iterative methods have been developed to try to overcome the problems of FBP, mainly the streak artifacts present in the final image. While FBP is based on the idea that there is only one possible solution to the sinogram reconstruction, iterative methods take into account the possibility that more than one possible reconstructed image could be available, which is actually much more realistic. The point is to choose which of the possibilities most resembles the real object, and this is done by computing multiple reconstructions and implementing an algorithm able to choose the optimal fit. The main idea that underlies iterative algorithms is summarized on

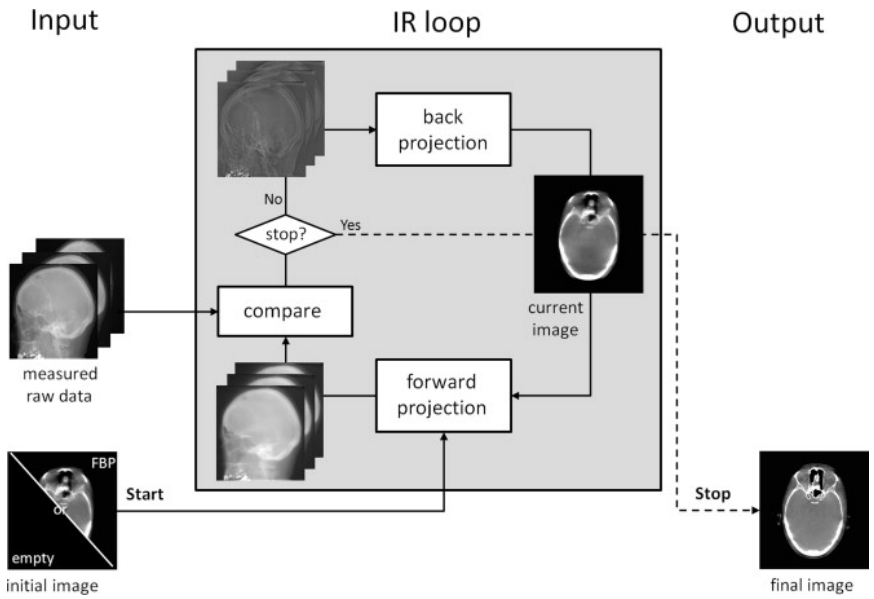

Figure 2.7: Iterative algorithms: flowchart [17]

Figure 2.7: these algorithms compute an initial guess of the reconstructed image, typically through FBP; this image is then forward-projected[1] and the estimated projections are compared to measured projections. The "error" between measured and estimated projections leads to the correction of the estimated object by means of addition or multiplicative factors. The corrected projections are then backprojected and forward-projected again, the new projections compared with the initial ones, ... and so on. The process comes to an end when the differences betweeen measured and estimated projections is sufficiently low: the stopping criterion and the optimization function make the difference between the different algorithms (i.e. Maximum Likelihood — ML-EM).
Iterative algorithms show improvements in noise reconstruction, are more able to handle missing-data situations and generally provide images of better quality. However, they are not free from drawbacks: the iteration parameters have to be carefully chosen in order to get good results and, most importantly, the computational requirements of these algorithms are more heavy than the ones needed to perform FBP. To this purpose, however, efforts have been made in order to speed up the process (e.g. with OS-EM). An overview on the different iterative reconstruction methods can be found on [18].

[1] Forward projection is the process opposite to backprojection: it leads from the image space to the set of projections.

Handling 3D data: 3D direct reconstruction and rebinning techniques

Positron Emission Tomography is one of the imaging techniques in which the shift from 2D to 3D imaging was most successful. In the 80s the first multiring PET devices were introduced: they showed thin septa of lead or tungsten between one ring and the other in order to avoid collection of coincident events between detectors which didn't belong to the same transaxial plane. However, it was soon made clear that collecting also LOR which were not parellel could have increased the overall count rate, improved the sensitivity of the scanner and, in turn, the quality of the images obtained: the septa that separated the detection elements became *retractable*, so that it would have been possible to switch from 2D to 3D mode with ease (Figure 2.9). Nowadays, most data collected from PET acquisition come from 3D mode.

The problem that immediately came out after the introduction of 3D modality was the reconstruction algorithm which had to be used: the classical 2D methods were no longer useful since data were coming from the 3-dimensional space. Two main paths were followed: the first to implement true 3D reconstruction algorithms (like 3DRP), the second to *rebin* the LORs, that is to sort them into ordinary 2D sinograms and then recover each 2D sinogram separately.

3DRP

True 3D reconstruction was the most obvious choice to reconstruct images from 3D data. Many algorithms have been studied in order to perform this operation, but one of the most effective ones was the so called 3DRP (also 3D-FBP) [19], an analytic direct three-dimensional reconstruction algorithm which tries to make use of all the information collected from a scan. In this section a very short and simplified explanation of its behavior is presented; for further information, refer to [19] and [20].

3DRP is based on Fourier convolution theorem, which requires the constraint of shift-invariance, that in turn can be interpreted as follows: only those LORs which reach the detectors with a polar angle bigger than a pre-defined θ_{min} are accepted. By doing so, any point source within the FOV would appear equally intense. This means that the brightness of the point source is invariant of its position within a certain angular range, which in turn leads to apparent spatial invariancy of the response of each detector. That is to say, shift-invariance is guaranteed if $\theta_{min} \leq \theta_{LOR} \leq \pi - \theta_{min}$, and only with this constraint Fourier-convolution theorem can be applied. 3DRP starts from this assumption, and extends it further:

1. a 3D image from the restricted number of LOR (i.e. LORs for which the angles are within the acceptable range) is formed

2. the resulting image is forward-projected in the remaining subset of projection planes (those for which θ_{LOR} was too small or too big), in order to estimate

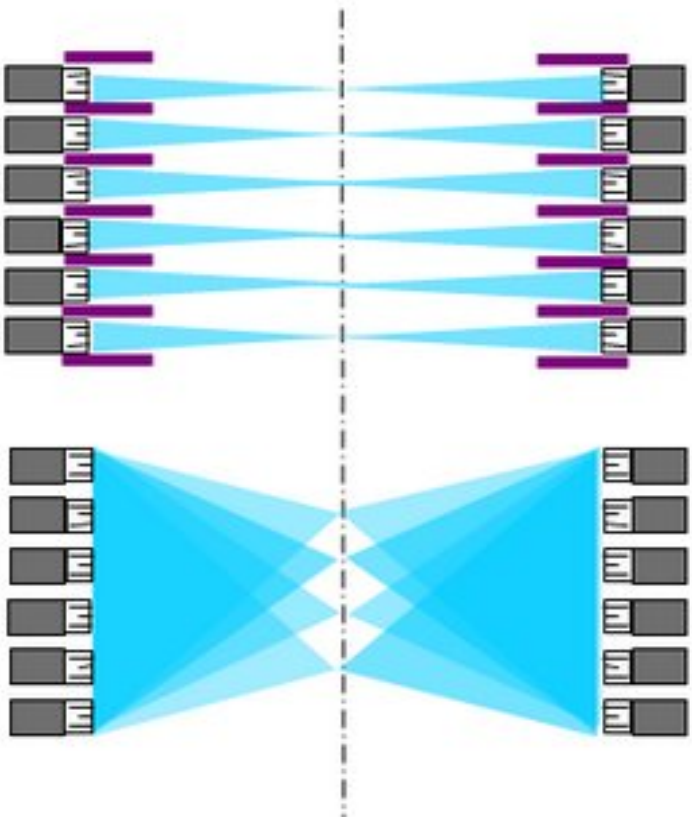

Figure 2.8: Difference between 2D and 3D PET modalities. Note the increased number of LOR generated in 3D mode: coincidences between any pair of rings are allowed. [3]

data not actually collected by the detectors and improve the statistics of the reconstructed image. In so doing, spatial-invariance is guaranteed even for those portions of detectors that previously didn't satisfy this requirement.

3. the newly estimated data and the original set of data are backprojected together, in order to obtain the final image.

Even from this brief and simple explanation, it is clear that direct 3D backprojection is complicated and time consuming, since a big number of LOR have to be processed at the same time. Other algotithms have been developed after 3DRP, but they weren't able to significantly decrease the computational time required by 3DRP [21]. This is the main reason why rebinning algorithms have been developed.

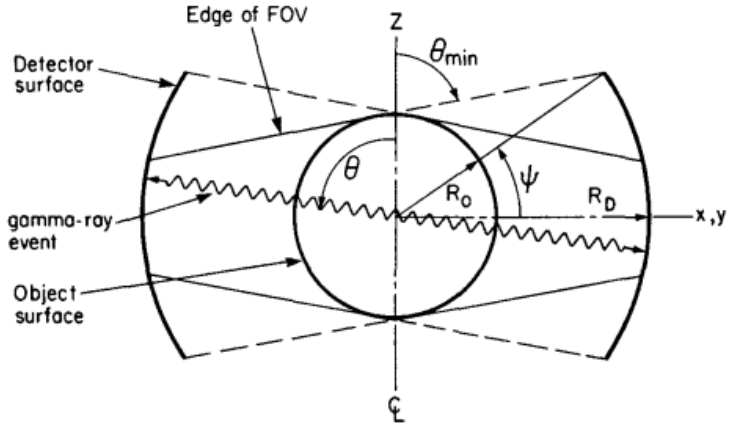

Figure 2.9: Cross section of two detectors and an object being scanned. In 3DRP, only those LOR which reach the detectors with a polar angle bigger than a predefined θ_{min} are accepted: in so doing, a point source moved in any point **of the accepted FOV** would show the same brightness.

Rebinning

As said before, the process of rebinning implies the sorting of LORs coming from the three-dimensional space into 2D projection planes, which are later reconstructed using one of the 2D algorithms described before. This process thus reconducts 3D reconstruction to several, faster-to-solve 2D reconstruction problems.
Among the main different methods used to perform rebinning, two of them are more common than others: Single Slice Rebinning (SSRB) and Fourier rebinning (FORE) — together with their respective variants (MSRB, FOREX, FOREPROJ, ...).
SSRB is the simplest rebinning algorithm that can be applied to a 3D set of LOR: it works by assigning the LOR to the slice that lies midway (in the axial direction) between the two z-planes in coincidence. Although approximate (it doesn't take into consideration the distinction between direct LOR —LOR that truly belong to that transaxial slice— and oblique LOR —which pass through various axial slices), this algorithm is quite fast (10 times more than 3DRP) and easy to implement. It works well expecially if the tracer is distributed in proximity to the central axis of the scanner.

FORE is a much more complicated algorithm which takes into account the distinction between direct sinograms (obtained when the axial spacing between the detectors is $\Delta = 0$) and oblique sinograms ($\Delta \neq 0$). Through a novel parametrization of the oblique LORs, it is possible to calculate the continuous Fourier transform P of each oblique and direct sinogram, for each polar angle; it was demostrated

that the inverse 3D Fourier Transforms of P lead to obtain the stack of rebinned sinograms throughout the whole axial space. Those sinograms can be reconstructed using any reconstruction algorithm. For detailed explanation on how FORE works, refer to [21].
In this work, because of implementative simplicity together with the fact that SSRB requirements were satisfied, single-slice rebinning was performed for all acquisitions.

2.4 Small-animal PET imaging: why?

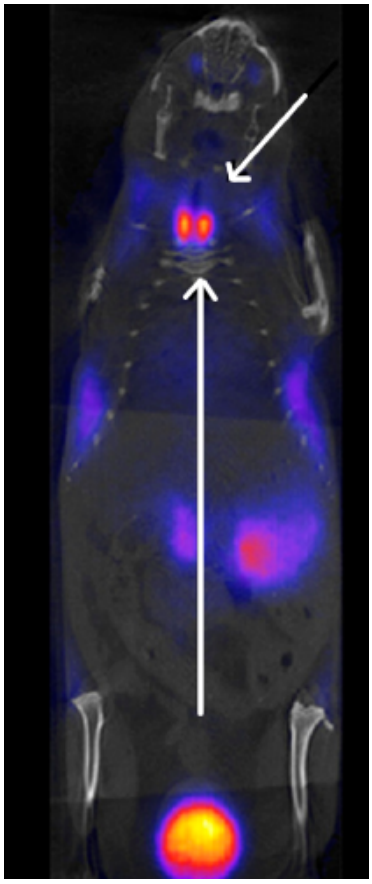

Figure 2.10: Coronal slice of SSRB OSEM reconstructed mouse, obtained with nanoPET/CT [9]. The level of accuracy is clear: the arrows show the two lobes of thyroid perfectly separated.

PET is a non-invasive imaging modality which has proved to be a useful and reliable tool in everyday clinical practice. It gives not only morphological, but also functional information on body parts or organs, and by consequence it is important in the medical field to diagnose tumors or malfunctionings. It is also in use in the research field to describe with more and more depth and accuracy biological processes, develop new and more efficient drug treatments and characterize development and progression of a disease.
Even considering all these positive aspects, traditional PET imaging still suffers from minor drawbacks: some *tumors*, for example breast cancer, need to be diagnosed at very early stages if cures want to be effective. This means that the device should be able to detect even malignant spots as small as 2 or 3 mm in diameter, if sufficient radiotracer is accumulated in such a small volume. Looking at pre-clinical applications, interest goes to *characterization of biological processes* that happen in small animals, like rodents and monkeys. Due to their reduced dimensions, a PET device should be able to resolve organs and structures very small and very close in space. Moreover, the *development of new pharmaceutical* products usually passes through a phase of animal experimentation. The exact knowledge of the processes that take place once the drug under test is injected would greatly speed up and improve the specificity of the drug production process. Finally, the field of *molecular imaging*, that aims

at understanding the dynamics and the kinetics of biochemical processes in vivo, evidently requires resolutions that can't be achieved by normal PET scanners (Figure 2.10).

These are the main reasons why, in the past few decades, the so called 'small animal PET cameras' have started to be studied and developed: characterized by small FOV and very high spatial resolution (down to 1mm or less), they are the perfect tool to reach all the objectives listed above.
The design of such devices has received a strong boost from the recent technological advances: better computing resources allow e.g. faster post-processing of signals; the progresses in material science and electronics helped the development of more efficient detection elements and faster readout and coincidence processing modules; progresses in computer science led to the introduction of new, more accurate reconstruction algorithms.

The process of designing a new small-animal PET device, however, is not free of obstacles and is still a challenge both for its hardware and for the software part. Results are so far encouraging, but the quest for the best camera, which mixes good performances with low costs, is still ongoing.

Chapter 3

Monte Carlo Methods in molecular imaging

Monte Carlo methods are a way to solve problems that involve stochastic processes: after creating a model of the physical system of interest, Monte Carlo methods simulate the processes and the interactions that occur in that system by random sampling the (a priori-known) probability density function of occurrence of that phenomenon. In the 60s, H. O. Anger was the first that tried to apply this method to simulate the physical response of his novel scintillation camera [22]; from there on, thanks to the fact that emission, detection and transport of radiation have a stochastic nature, Monte Carlo-based simulations have become very popular in the field of radiation medicine. A boost to the use of Monte Carlo-based methods came in the past few years, with the higher computational capabilities and faster execution times allowed by modern computers.
Speaking about medical applications, Monte Carlo methods are useful to quantify and describe radiation amounts in order to do better radiation protection, to plan reasonable treatments in radiation therapy, to reconstruct and model the behavior of devices used both in diagnostic radiology and in molecular imaging, to optimize scanner design and protocols. All of this can be done **without the need to build a real machine** (expensive) **or to take tests using real patients** (possibly dangerous).
Considering simulations of new medical devices, Monte Carlo methods can accurately describe the physics of interaction of particles with matter. Best of all, they allow to change different parameters during the simulation, thus giving the possibility e.g. to test different geometrical configurations or modules arrangements – an approach that sometimes would be impossible or too expensive to carry on with real experiments or analytical calculations. By means of simulations, it is therefore possible to test very different or completely innovative machines at low costs and with high reliability. If the simulation gives good results, it will be relatively easy to build the real camera.

The software used for this project has its roots on Monte Carlo simulation of particles' behaviour. Hence, in this section, a brief explanation on how Monte Carlo methods work is presented. In Section 3.2, particular attention will be given to the software package (GATE) used for our simulations.

3.1 The general idea: how Monte Carlo methods work

In the field of particle simulation, the idea is to take a particle, that can represent an electron, a positron, an ion,... and track its path inside the device under the influence of an electric field and\or of scattering mechanisms. This is done for a lot of particles and, for each one, their average properties (velocity\energy\position\...) are computed. The more events are simulates, the better the quality of the reported average behavior of the system, the lower the statistical uncertainty of the model. In brief, this is a simple description on how Monte Carlo simulation works considering, for example, an electron travelling in a medium: the electron, that has some energy, some momentum etc, starts moving under e.g. an electric field following the equations of motion, until a generic scattering event occurs. It is important to figure out how the energy, the position and the momentum of the particle have changed just after the collision. A Monte Carlo simulation algorithm goes through the following steps, that have to be performed for each particle being simulated:

1. An electron is chosen and it is followed while it freely moves in a medium for a certain time; position and momentum are calculated just before the collision $\Rightarrow r1$

2. The algorithm randomly decides what scattering event occurred, according to the probability distribution of all the scattering events available $\Rightarrow r2$

3. Energy and momentum of the particle are updated at tc+ $\Rightarrow r3, r4$

4. The tracking process starts all over again, and is repeated for many particles

The values for r1(collision time), r2 (scatter event), r3 and r4 (polarization angle and azimuthal angle of the new momentum vector) have to be chosen randomly by the algorithm, according to a-priori known probability distribution of each of those events. Later, it will be necessary to make a proportion between this probability P of random numbers ($0 \leq P \leq 1$) and e.g. real collision times, in order to get the actual value for r1. The same happens to calculate r2: knowing the contributions of the different scattering mechanisms at some particular energy and normalizing them to 1, depending on where the random number generator lands, leads to the determination of what scattering event terminates the free flight of the particle. An approach similar to the one just explained is performed when choosing r3 and r4. In conclusion, the idea is to track every particle for Δt and after that collect statistics for that particle at a particular location; statistics are then updated, the particle is made go again for another Δt and so on, for each particle simulated.

3.2 Monte Carlo methods in nuclear medicine: GATE

Simulations of PET devices are based on the principles briefly described before: each of the particles generated by a virtual, radioactive source is simulated and its positon, energy and interactions are registered.
There are two different approaches used to simulate particles and devices in nuclear medicine field.

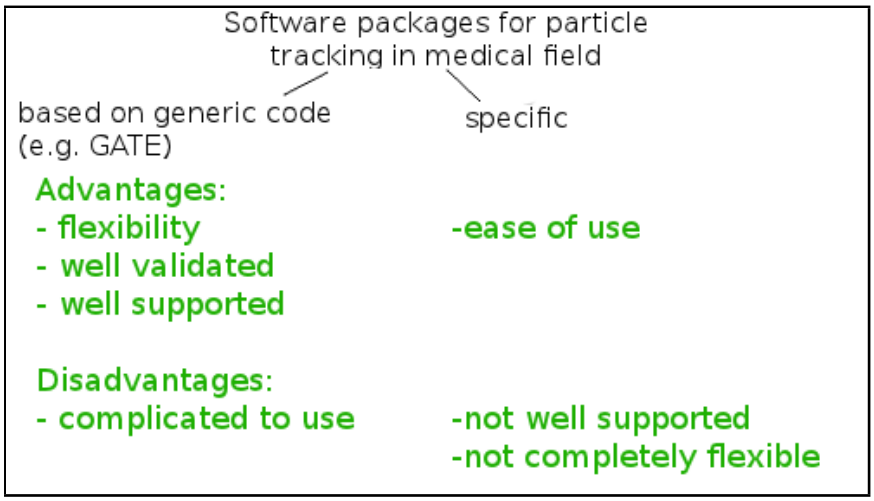

Figure 3.1: The two software categories used to track particles in nuclear medicine: main advantages and disadvantages. Software can be either based on codes written for generic particle description (e.g. GATE, which is based on Geant4) or it can be specifically tailored to nuclear medicine applications.

The first approach makes use of *general-purpose* simulation codes for particle tracking, like GEANT4, EGS4, MCNP, ... They allow users to handle a wide range of well-validated physic processes, geometry modelling tools and visualization utilities [23]. Hence, users can accurately simulate particle transport and associated phenomena, tailoring the tracking to their specific needs; for example, they can choose the phenomena that are of interest and leave out those that are negligible to the specific application. It is evident that this generic-code approach has a certain number of advantages, among which flexibility, accuracy and reliability. Moreover, a good number of users and developers uses these generic-code software packages, and documentation and support are thus extended. The main disadvantages of these general purpouse simulation codes is their complexity, together with the fact that they are quite slow and that programming is harder, since the user has to carefully specify every detail of the process(es) to be simulated. Moreover, sometimes it is difficult to adapt those generic codes to specific needs,

like biomedical applications.

The second approach is to use *dedicated* simulation software, such as PETsim, SimSET, Eidolon,. . . .These software packages are specifically created for nuclear medical imaging applications, and therefore they are easier to use and the processes are faster to simulate. On the other hand, since they are more specific, they don't have the same flexibility as generic codes(e.g., they have a limited choice of geometries or physic processes among which the user can choose), and this could be a limitation in trying to model completely innovative scanner geometries. Moreover, these software packages require, as for every software, continuous manteinance and upgrades: however, since they have been developed by small groups of researchers and\or companies, support is not always given for granted. Finally, they can not rely on a wide community of users nor on good documentation and manuals. [22]

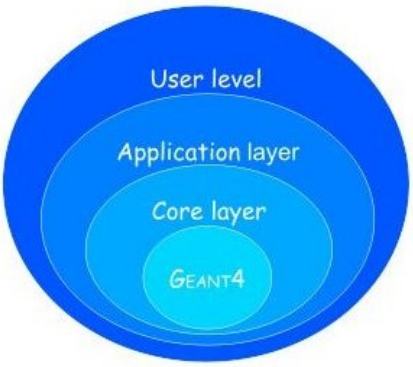

Figure 3.2: Layedred structure of GATE software package [24]

In this work GATE software has been used. GATE (Geant4-based Application for Tomographic Emission) is a simulation platform for PET/SPECT applications based on Geant4, a non-specific C++ software for high energy particle-tracking. GATE has been developed in order to provide a user-fiendly tool to help the design of devices in the field of nuclear medicine, filling the gap between accurate particle tracking and biomedical applications. It includes specific features useful for molecular imaging simulations(for example, a database containing the most commonly used materials, pre-defined sources, possibility to choose readout levels, ability to manage time and movement), and allows the final user to define, among all, scanner geometries, physical processes involved, sources, phantoms of any size and shape, acquisition configurations, duration of the acquisition, output to be generated.

GATE: advantages and disadvantages

GATE has two main advantages: it is object-oriented and script-based. The object-oriented feature leads to great flexibility, since modules and submodules can be variously combined together in order to design almost any scanner geometry we can think of, from small rectangular detectors to multi-ring arches. Moreover, this feature makes the code re-usable and able to be adapted from one context to another in a fast and easy way (for example, through the use of 'repeaters').

The fact that GATE is a script-based toolkit, on the other hand, means that the final user doesn't have to know C++ in order to proceed with the simulation design. Figure 3.2 shows GATE's layered architecture: the core layer contains the classes that define which tools are available (Geant4 classes, written in C++, plus additional GATE classes used for geometry definition, time management, source definition) and how they can be used. The application layer is an extensible set of C++ classes based on the GATE core, that allows to define volume geometries or movement modules. On top of the application layer is the user layer, where final users can simulate experiments using a modified version of the Geant4 scripting language. The *command interpreter class* makes it possible to "translate" the script commands into a specific C++ function provided in the core or application layer.

Chapter 4

The ten-detectors camera simulation

The aim of the present project is to simulate and evaluate the performances (resolution in space, uniformity, counting rate, scatter fraction) of a modular PET scanner, with the ultimate goal to find a lower bound to the number of detectors that could guarantee good results at the same time. These simulations will thus make evident either if removing 2 detectors from the previously evaluated miniPET II [1] is feasible or if the use of 12 detectors represents a lower bound to detector number, under which performances become unacceptable for a small-animal scanner. In fact, the choice of the ring diameter and of the number of detectors is often crucial and it could deeply influence costs and performances of a PET apparatus. To this purpose, knowing the encouraging results obtained from miniPET II [1], the number of crystals of this camera was set to ten and tests were carried on in order to check these features and compare them with the 12-detectors design.
In the first part of this chapter, a detailed explanation of the simulation outline is given. Afterwards, the tests performed to check the 10-detectors geometry are presented.

4.1 The macros

In order to run the simulation, two alternative ways can be followed: the first one is to launch the simulation software and write one script-like command at a time. The other alternative is to write a sequence of commands in a text file, called *macro*, that can be written "off-line" and then launched all at once in GATE, using a specific command. This approach has the advantage of being less time-consuming and more practical when it comes to debug the simulation itself, because it allows to edit only the wrong line and then re-launch the whole macro, without having to start from the beginning every time. In the present work, the simulation has actually been divided into a main macro and several different submacros, which are

called in order of appearance from the main macro. In the following section, a brief explanation of the content of each macro is presented.

Visualization

One of the first things that can be done is the **visualization** of the camera being designed; this step is of particular importance when it comes to debug the simulation itself and find any possible mistakes in the design of the machine. However, it is not really useful while the simulation is running; on the contrary, it considerably slows down the simulation time, especially when tracking of particles is enabled. This is the reason why, in this work, visualization was almost always kept disabled. In the visualization file it is possible to set the viewing angle, the zoom or the visualization style of the camera. Modifications at this level only affect visualization, not the actual positioning/dimensions of the device being simulated.

Geometry

The structure (or **geometry**)of the camera is then designed. In GATE, the definition of the geometry of the camera is hyerarchical and consists of different levels: we start from the definition of the main shape of the scanner (cylindrical, rectangular, ...) and go down with the creation of the detector module(level 1), inside which smaller detection elements can be inserted(level 2), like a Matryoshka. The number of levels available depends on the type of the scanner.
In this work, the choice to use a CilindryicalPET is determined by the fact that this scanner geometry is especially thought for PET scanners. In fact, only with this type of geometry GATE is able to store coincidences.
The cameras here simulated are both cylindrical; one of them (***r77-miniPET*** from now on) has a radius of 77 mm, while the other (***r106-miniPET***) has a radius of 106 mm. Both cameras are made up of 10 detector modules, but in **r106-miniPET** they will be more spaced between each other, due to the increased diameter.
Each detector consists of a 35x35 array of crystals.
Each crystal measures $1.27x1.27x12mm^3$: these values have been chosen according previous literature concerning small-animal miniPET, and they have been verified with two simple simulations using 2 detectors and a point source.

As for **crystal thickness** (12 mm), the distribution of hits throughout the crystal was observed: it was noted that 50% of the hits within the energy range occur in the first 6mm for BGO and 7.26mm for LYSO. It is well known [12] that the thinner the crystal, the lower its detection efficiency, the lower the singles' count rate. Therefore, a too thin crystal would lead to a low rate of detected coincidence events and, in turn, to poor image reconstruction. On the other hand, thicker crys-

tals —as shown on Figure 2.5 on Chapter 2— are more likely to produce parallax errors (due to DOI uncertainty), which would increase the noise and reduce the resolution of the final image. In brief, the resolution improves by decreasing the crystal thickness, but the count rate increases by doing the opposite: the choice of the ideal thickness is a compriomise between those two opposing needs. The 12-mm value was considered to be a good choice.

As for the other dimensions of the crystal, the **front side** of 1.27 mm is sufficiently small to guarantee a sharp detection response function. Moreover, this value is good because it is bigger than the fundamental limit of PET spatial resolution (0.81 mm, see Chapter 2) [6]: a crystal whose front side was lower than 0.81 mm wouldn't offer any benefits in terms of spatial resolution. On the contrary, it would be more expensive and its fraction of scintillating volume would be reduced.
No DOI corrections were applied, since the objective was to keep the device simple and, possibly, low cost. The pitch between the crystals is 1.35 mm.
Full specifications of the simulated scanners are given in table 4.1.

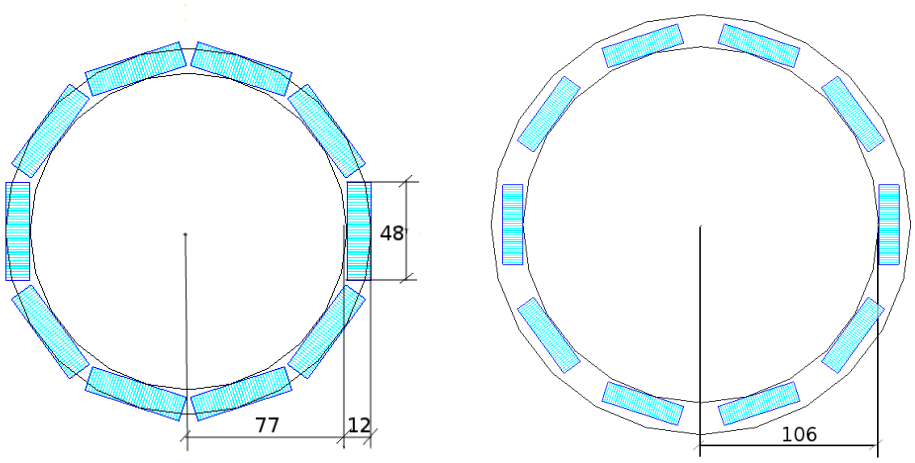

Figure 4.1: Picture of the cylindricalPET system composed of 10 detectors and 1225 crystals (35x35 array) per detector. From left to right: frontal view of first camera (A, r=77 mm); frontal view of second camera (B, r=106 mm). All values in mm.

Phantoms

After defining the geometry of the scanner, a **phantom** that simulates the imaged object has to be defined aswell. Four different phantoms have been used in this work: two *scatter* phantoms of different diameters (*mouse-like* and *rat-like* phan-

	r77-miniPET	r106-miniPET
Axial length [mm]	50	50
Ring diameter [mm]	154	212
No. detectors	10	10
No. crystals/det	35x35 (array)	35x35 (array)
Crystal element size [mm]	1.27x1.27x12	1.27x1.27x12
Crystal material	LYSO	LYSO

Table 4.1: Geometrical properties of simulated scanner geometries

tom), used to test the scatter fraction and the scattering properties of the camera, a *point* phantom and a *derenzo* phantom. Details on each phantom are provided in the following section ("The tests", 4.2).

Physical processes

After setting up the camera, the **physical processes** that will occur during the simulation are defined. Four processes can occur when an electromagnetic wave (like a gamma ray) interacts with matter [12] :

1. **Photoelectric effect** happens when a photon interacts with an electron of the hitted material. The photon tranfers *all of its energy* to the electron, which in turn is ejected from the atom. This process may occur in the object being imaged and it is the basis of interaction in the crystals.

2. **Compton scatter** occurs when a photon hits an electron and ejects it from the atom it was bounded to; the photon doesn't completely loose its energy and can keep on travelling in the scattering medium, until all of its energy is lost. The energy of the scattered photon depends on the scatter angle and on the energy of the incident photon [12].
   Even if this effect is not desirable, neither in the detector nor in the phantom, it is one the predominant phenomena when talking of interaction between gamma rays and matter in the PET energy range.

3. **Rayleigh scatter** is more infrequent and usually occurs at low energy levels, but it was included in order to make the simulation more realistic.

4. **Pair production** was not considered since it can only occur at high energies (at least 511×2 keV). This energy value was never reached in our simulations, especially considering that an upper energy threshold of 650 keV has been applied in all of them.

As for photoelectric and Compton effect, the GATE-provided *Standard model* was used to describe and track the physics of the particles (this was done because

the energy range is around the usual working range), while the so called 'Livermore Model' (GATE v.6.1; "lowenergy" model in GATE v.5) was used to model Rayleigh interactions, that in fact occur at low energies.

Once geometry, phantom and physics are defined, initialization must be performed: the initialization process builds up the camera and generates the parameters needed to simulate the physical processes listed above (mean free path of the particle, energy, ...). After initialization, two more components have to be included before making the simulation run: the digitizer and the sources.

Digitizer

Setting up the **digitizer** turned out to be one of the most crytical parts of the whole simulation, and actually it is the one who gave the most interesting results during the work; all parameters have to be carefully considered in order to produce results that are reasonable, comparable with previous works and realistic.

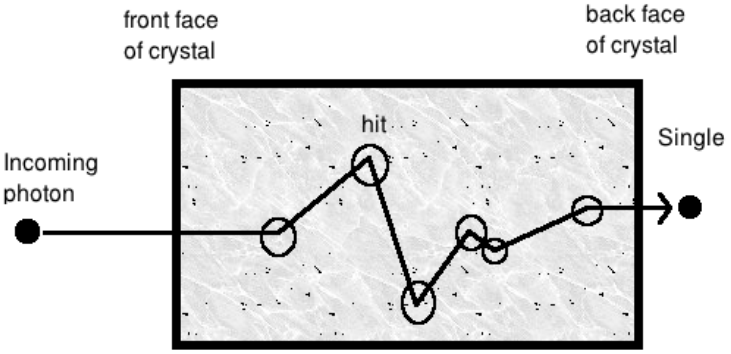

Figure 4.2: Hits and singles within a crystal. Hits represent all the physical interactions occurring in a volume; for each of them energy, momentum, position and interaction type is stored. A single is obtained by considering the history of all hits and integrating them into a set of final physical observables –like real electronics would do.

First of all, a few words have to be spent on what a digitizer is. Gate offers the possibility to collect *hits*, *singles* and *coincidences* (Figure 4.2). While hits store interaction information between the particle and the material, they are not the output that is actually detected at the opposite side of the crystal. The role of the digitizer is to simulate the real behavior of the detector and to build, from the hit information, a cumulative set of physical observables (final energy, position, time of

detection, ...). Each *single* carries information about these physical observables. Hits and singles haven't been collected in this work, since the information we need comes all from the coincidences. However, coincidence analysis is based on singles, since a coincidence is in fact defined when two singles hit two distinct detectors in the same time window. In this work, the digitizer includes the following modules:

- *adder*: since the particles hitting each crystal can interact more than once with it, and since the real electronics is not able to distinguish between them (it only calculates an integrated signal), the adder module just sums up all the hits occurring in the same volume to produce a single pulse. To be detailed, GATE manual says that the energy of the single is the sum of energies in each volume, the position is obtained as an energy-weighted centroid of the different hit positions and the time is the one at which the first hit occured [24].
  The *adder* module is necessary if we want to simulate a realistic machine.
- *readout*: this module sets the geometry level at which the singles are read. In our case, the detector was considered as the level where the electronic readout takes place: this means that the energies of all the singles hitting all the crystals are further summed up at this level. This reflects the behavior of real machines, in which the Position-Sensitive Photomultiplier Tube (PSPMT) is usually shared between many crystals (typically, one PSPMT per one thousand crystals).

In the first simulations that have been run during these months, a lot of parameters had been set in order to fully describe the light/energy properties of the LYSO crystals used: *transfer efficiency, light yield, intrinsic resolution* modules were included to better simulate the properties of the material the crystals are made of. In this case, the crystals are made of LYSO and the parameters had been set as follows: transfer efficiency coefficient= 30%([25]), light yield= 33800 quanta/MeV([26]), intrinsic resolution= 8.1% ([26]). However, since the main purpose of the project is to simulate in first approximation how the camera works, and to compare the results with the miniPET II, these software modules that added extra details were substituted with some more useful modules, such as the ***energy blurring*** module and the *deadtime* module – the only ones that were used in the 12-detectors' simulation. The first one (blurring module) is introduced because the real crystals are not able to detect the actual energy but have a certain resolution of each energy level: in the present work, a resolution of 26% was used at 511keV; this value comes from the simulations performed with the 12-detectors camera, which in turn had been set after measuring the real energy blurring of the same camera (with real LYSO crystals + H9500 PSPMT and real electronics). The **deadtime** module, on the other hand, mimics the behavior of the electronics: if two pulses reach a crystal in a too short period of time, it is possible that the second one goes lost,

only because the detecting electronics and the PMT are not able to distinguish it from the previous one. This loss of detected particles lasts a certain amount of time, depending on the characteristics of the detectors used as well as of the read-out electronics. The "paralyzable" option set for this module assumes that *each* photon reaching the PMT prevents further detections for the same amount of time. In our simulations, deadtime has been set to 200 ns: this value was chosen according real measurements done with the detection elements of miniPET II. See subsection 5.1 to see how the deadtime influences performances.
Other modules have been included in the digitizer. First, a ***low and high energy cut*** module, used to threshold the singles and consider as valid only those ones whose energy falls into a pre-defined energy window, was introduced. Previous literature [1, 27, 23] shows that a good choice is to set the low enegy cut at 350 keV and the high energy threshold at 650 keV. These values represent a good compromise: allowing too low energy photons, that may have interacted too many times with matter, would increase the noise of the image without adding any useful information. On the other hand, there is the slight probability that the process of ^{22}Na decay produces gamma rays with energy higher than 1 MeV (1.275 MeV): those (unwanted in PET) rays could go through Compton interaction and thus increase the total amount of random coincidences detected. For these reasons, only the rays whose energy was included in the [350-650] keV energy window have been considered in this work.
Secondly, the filtered pulses were analyzed by the ***coincidences*** and ***delayed coincidences*** modules. The coincidence analyzer searches in the list of singles for those that are detected within a given time interval (the so called 'coincidence window').In this work, coincidence window was set to 3ns (according to previous work on miniPET II [1]). Random, scatter and multiple coincidences are of importance in determining the performance of the scanner: as suggested in numerous sources of literature, i.e. in [12] and [3], the number of random events can be measured by introducing a time delay in one of the two channels of the coincidence circuitry, based on the fact that coincidences that are registered when one of the two detectors is time-shifted are interpreted as random for sure. In this work, the same coincidence window was kept for randoms (3ns), while the delay time was set to 500 ns. As for multiple coincidences, GATE offers the possibility of choosing between different *multiple policies*: in this simulation, if more than two singles occur in the same moment, the coincidence event that is stored is the one coming from the two pulses with the highest energy (*takeWinnerOfGoods* policy). Scatter coincidences are calculated by making the phantom *sensitive* (that is, able to store the interactions occurring within it).

Minimum sector difference

A few words have to be spent on a particular parameter encountered in defining the last two coincidence modules, the ***minimum sector difference*** parameter: only

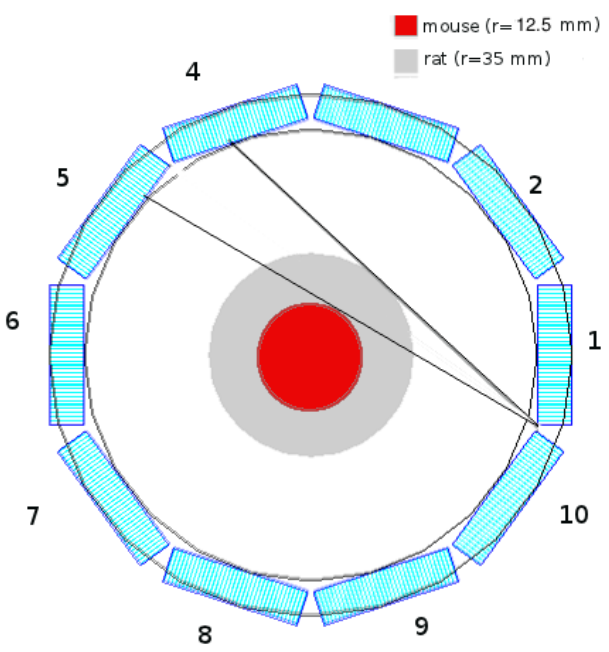

Figure 4.3: Simple sketch used to calculate the value of **minSectorDifference** parameter. Red: mouse-like phantom; grey: rat-like phantom. The black lines draw the extreme LOR that can be formed by each phantom: in rat-like case, the maximum difference betweeen detectors, in order to get a good coincidence, is $4 - 1 = 3$=minSectorDifference. All coincidences betweeen, e.g. , detector 3 and 1 are coming from scatter events and therefore ignored.

if the 2 singles are separated by a number of detectors greater than or equal to the minSectorDifference value, they are considered to form a good pair; otherwise, the coincidence event will be rejected. The choice of the minSectorDifference value has to be careful: for a 12-detectors-camera, this parameter can be conveniently set to 4 beacuse in this way, knowing that scatter in the phantom usually occurs at wide angles, it is possible to filter the good coincidences from the ones most probably coming from a scattering event. However, this value (4) is not appropriate for the 10-detectors camera, since in this way we would remove more coincidences than needed (and, most importantly, even good ones), and the default value (2) allows too many coincidences to be recorded. From a simple sketch of the geometry (see figure 4.3 for details), and considering a maximum phantom diameter of 70 mm, a more suitable and reasonable value for the camera being simulated in the current job is minSecDifference=3.

4.2 The tests

Once the structure of the camera was designed and the physical processes were set, it could be possible to test the performances of the new geometry. Plenty of tests can be performed in order to assess if the camera is doing well or not, but there are some that are more important than others. Founded in 1926, the Association of Electrical Equipment and Medical Imaging Maufacturers (NEMA) provides technical standards in various fields of engineeering, included the one of medical imaging. Among all, its members study which are the most significant tests that can be performed to fully describe a new PET apparatus and which is the best way to perform them, in order to define a standardized procedure. In so doing, the results are simple, clear, and can be easily compared with the ones obtained from other studies.

In this work, the attempt was to design tests that were as similar as possible to the ones advised by NEMA for small-animal PET devices [5]. The tests with which the 10-detector PET has been evaluated are the following:

1. scatter fraction and count rate performance
2. sensitivity, axial and radial
3. spatial resolution (FWHM)

Moreover, in order to check the quality of the images obtained, a test using a *derenzo phantom* was done: although it is important to underline that this test is not included in the NEMA standard, it is a common way to depict the imaging performances of the camera at a glance.

Scatter fraction and count rate performance

As stated in Chapter 2, it is important to understand the fraction of scatter and random coincidences with respect to the total count rate. In fact, scatter coincidences add backgound noise to the image, decreasing its overall contrast. Random coincidences also produce errors in the count rate and, since they do not contain any spatial information, they can lead to significant artifacts in the reconstructed image [28]. To determine the amount of these two quantities, the scatter test was set this way: a scatter phantom was positioned at the center of the FOV of the camera. According to NEMA standards, the scatter phantom is a polyethylene cylinder (predefined high density =0.96 g/cm^3) that covers the whole axial FOV (height=50 mm).
Since scatter fraction increases with the volume of the object under examination, phantoms of different diameters have been used: the first is a *mouse-like* phantom, whose diameter is 25 mm, and the second is a *rat-like* phantom, with diameter=70 mm. A 50-mm-long ^{18}F line source is inserted in each of the phantoms, at a radial distance of 10 mm and 17.5 mm from the central axis respectively. Acquisitions at

different levels of activity were performed for 120s each; the acquisition time was set this way in order to have a significant number of coincidences ($>10^6$) while keeping the size of the output files reasonably small. The simulations were performed at different activity (A) levels, starting from A=5MBq up, at 10MBq intervals. They were stopped at A=90MBq because it was noted that, after this level of activity, the count rate for the **r77-miniPET** had considerably decreased and the trendline was already well-shaped. Exceptions were made for the rat phantom and for **r106-miniPET**, for which simulations were stopped at 100MBq. For each activity level, a Matlab program specifically written was in charge of evaluating the number of prompt, true, scatter and random coincidences; according to NEMA requirements, the Noise Equivalent Count Rate (NECR) was also evaluated, since it is a good way to measure the actual capabilities of the camera, removing the influence of scatter and random coincidences.
Prompt counts were calculated as the total number of events collected during each simulation. Random events were obtained by setting up a delayed channel (delay=500ns), according to the 'delayed channel method' (Chapter 4, Section 4.1, digitizer module). The ASCII output of the simulations contains information on where scatter events have happened (if any): scatter coincidences were evaluated by counting the coincidence lines in which one (or both) photons had been deviated in the phantom, after annihilation had occurred. Scatter fraction (SF) was subsequently evaluated as

$$SF = \frac{s}{s+t}$$

where s=number of scatter coincidences and t=number of true coincidences [29]. Finally, NECR was calculated according to the formula expressed in [30]:

$$NECR = \frac{t^2}{s+t+2kR}$$

where R=number of random coincidences and k represents the volume occupied by the phantom with respect to the total volume of the camera ($k = \frac{d_{phantom}}{D_{FOV}}$).

Sensitivity

For both spatial resolution and sensitivity, a point source has been used: it is 0.3 mm-diameter sphere of ^{22}Na, inserted in a plexiglass cube of 10.0 mm extent on all sides [5], whose activity was set to 48 kBq. For both spatial resolution and sensitivity measurements, the source was moved at specific positions within the FOV of the camera: the positions were chosen according to NEMA recommendations.

Sensitivity is defined as *the number of counts per second detected by the device with respect to the total activity of the source* [31]. Since the count losses become more and more evident in moving the source from the center to the axial edges of the camera, the first test that was performed was to check the **axial sensitivity**

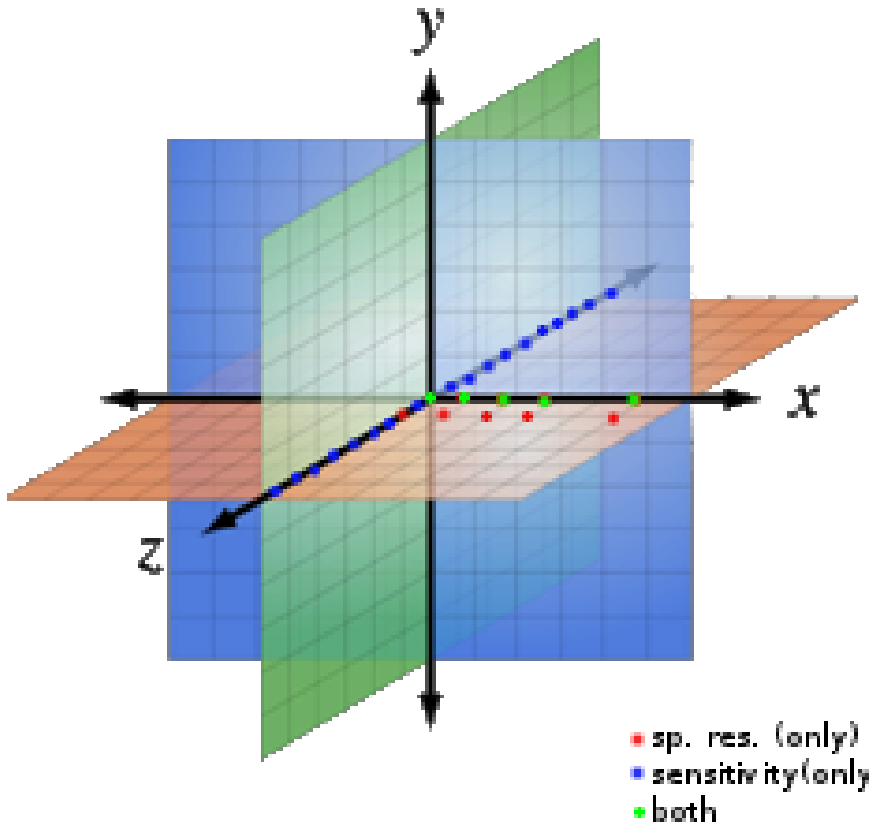

Figure 4.4: Positions at which spatial resolution and sensitivity were measured. For **axial sensitivity** (blue), the source was moved along the central axis of the camera with steps equal to the crystal pitch(1.35 mm), for a total of 35 acquisitions. **Radial sensitivity and spatial resolution** (green) were measured by positioning the source at different radial positions along the FOV: 0mm, 5mm, 10mm, 15mm, 25mm from the center of the camera. Further tests to assess **spatial resolution** were done with source at 1/4 of the axial FOV (red).Note 1: due to space issues, in the figure only 20 positions for axial sensitivity are drawn. Note 2: not in scale.

of the camera, that is how the count rate changes along the z-axis. The source was therefore moved along the central axis of the camera, as described on Figure 4.4. Acquisition lasted 60 seconds each (120s for r106-miniPET): this time window fulfils NEMA requirements, since it allows to collect more than 10^4 events. The starting activity of the source was kept low (48 kBq) so that the influence of scatter coincidences was negligible (<5%) [31] (random coincidences were almost absent, since the source is practically dimensionless).
Following analogous principles,**radial sensitivity** was measured by moving the same puntiform source along the x direction.

Spatial resolution

Spatial resolution represents the ability of an imaging device to distinguish two high-contrast, adjacent objects. One way commonly used to describe spatial resolution is to analyze the point spread function (PSF) of a point source: if the source is point-shaped, in an ideal case this would produce a PSF that is one single spike.

However, in real simulations, the source isn't perfectly puntiform and many effects can concur and worsen the spike-shaped ideal PSF. One way that is commonly used to assess spatial resolution is to calculate the Full Width at Half Maximum (FWHM) and the Full Width at Tenth Maximum (FWTM) of the PSF, both along the axial, the transaxial and the radial direction. This procedure is also recommended by NEMA.
In our simulations, the point source is the same as the one used to assess sensitivity, that is a 0.3mm-diameter sphere, filled with ^{22}Na and embedded in a Plexiglass cube of 10.0 mm extent on each side. This source was positioned at different radial positions (see Figure 4.4), and the same tests were taken at 1/4 of the axial FOV (-11.81 mm from the center). The activity of the source was 48 kBq and simulations were taken for a time that was sufficient to collect around 10^5 prompt events: 300s for **r77-miniPET** camera and axial offset=0, 420s if axial offset was -11.81 mm. As for **r106-miniPET**, acquisition times were 420s and 600s respectively.
Coincident events were collected in a ASCII file as a list of events; a Matlab code was written in order to go from this list of events to the sinogram (see Chapter 2). Later, the sinogram was used as input of Matlab 'iradon' function, that performed Filtered Backprojection of the sinogram. The other input parameters of this function (number of projections and filter used) had to be carefully chosen: as for the number of projections, the 0.86mm gaps between detectors that the geometry inevitably produces require a finer angular sampling. This led to set the number of angular projections to 560, so that each bin included LOR whose difference in inclination was lower than 0.32°. Setting the number of angular projections to a higher value wouldn't produce any differences in spatial resolution values while, if this number was lower, the difference would become significant. In fact, setting the number of angles 180° and leaving all the other parameters unchanged would produce a FWHM along Y of 1.90mm; this value is 16% higher than the one obtained with the 0.32° (180°/560) angular step. As for the filter used, the one that

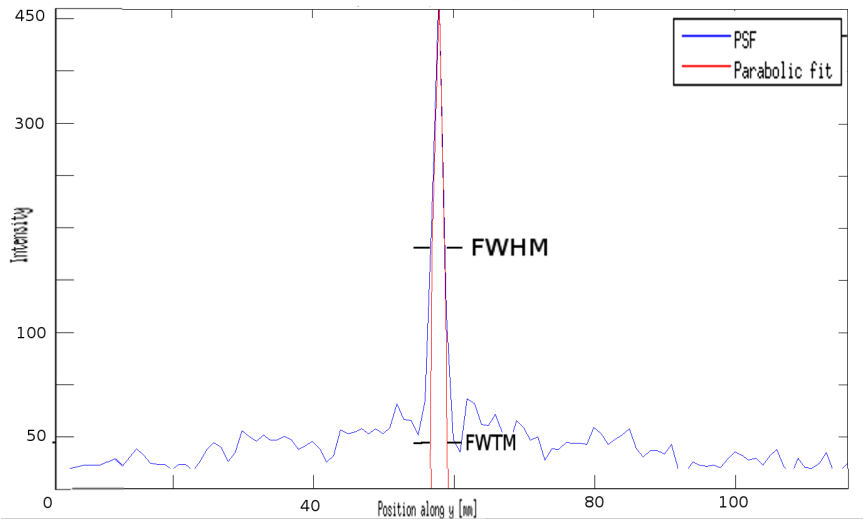

Figure 4.5: Example of PSF and parabolic fit of a point source located in the center of FOV (NEMA standard). Position along y is in [mm].

preserved high frequencies best was chosen, in order to keep good trace of the edges of the source and obtain images as sharp as possible: the 'Ram-Lak' filter was the one that best accomplished this objective, despite the more noise it leaves on the image.

The images thus obtained were processed according to NEMA recommendations: for each direction of measurement, the sum of the intensity values along its parallel direction was taken, and a one-dimensional intensity profile was obtained. Data were later fitted into a parabole, whose parameters were calculated using the peak point and the two nearest neighboring points. The parabole thus obtained was interpolated with a finer grid (.01 precision) and FWHM and FWTM values were calculated for all the three orthogonal directions (Figure 4.5).

Image quality

Closely related to spatial resolution are the results obtained from image quality tests: to this purpose, a Derenzo phantom has been used. This phantom is not included in the NEMA recommendations, but it is commonly used to visually describe the properties of a PET device, including both image quality and spatial resolution: it is a 50-mm diameter, polyethylene phantom, in which holes of different diameters have been drilled (Figure 4.6). Each of these cylinders was filled with a ^{18}F-line source, whose activity was proportional to the volume of each rod (5

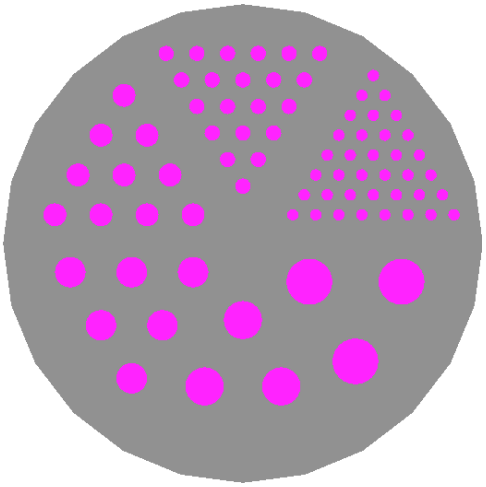

Figure 4.6: Front face of Derenzo phantom used in our simulation. The diameters of the holes range from 1.2 mm to 4.8 mm (1.2mm, 1.6mm, 2.4mm, 3.2mm, 4mm and 4.8mm). The height of the phantom covered the whole axial FOV(50 mm).

μCi/ml). The phantom was positioned at the center of the camera and acquisitions of it were taken for 30 minutes, in order to collect a sufficient number of prompt coincidences (more than 10^7 coincidences for **r77-miniPET**, half of this value for **r106-miniPET**).

Chapter 5

Results, discussion and comparison

The simulations of **r77-miniPET** gave encouraging results, while **r106-miniPET** proved to have worse performances. Even if it was clear from the scatter tests that r=77mm was the best choice, all the tests were carried on even for **r106-miniPET**. This also allowed to demostrate with more evidence some of the effects that occurred in **r77-miniPET** design (e.g. geometry effects on spatial resolution).

5.1 Results

Scatter fraction and count rate performance

The results of count rates tests are presented on Figure 5.1 and 5.2: it can be observed that count rates for **r106-miniPET** are lower than the ones obtained with **r77-miniPET**, and this could be explained by the fact that the free space between the detectors determines losses in coincidence detection. Moreover, in **r106-miniPET** the peak count rate is reached at a higher level of activity.

A table summarizing the values obtained, together with the corresponding activity levels, is on 5.1. The SF value of the **r106-miniPET** is slightly lower and the peak is reached at higher levels of activity: this could be a point in favour of the r-106 geometry; however, the count rate in this kind of geometry is lower at low levels of activity, and this could be a drawback when trying to image less active(but still potentially dangerous) areas.

The effects of deadtime

Deadtime turned to be a very delicate parameter to set. As said in the previous section, deadtime is the time that the detection electronics needs to recover and be ready to process a new event, after one has been stored. This means that, if two coincidences occur too close in time one another, it can happen that the electronics isn't able to record the second event, that subsequently will be lost. The deadtime value depends on the components being used and can greatly affect

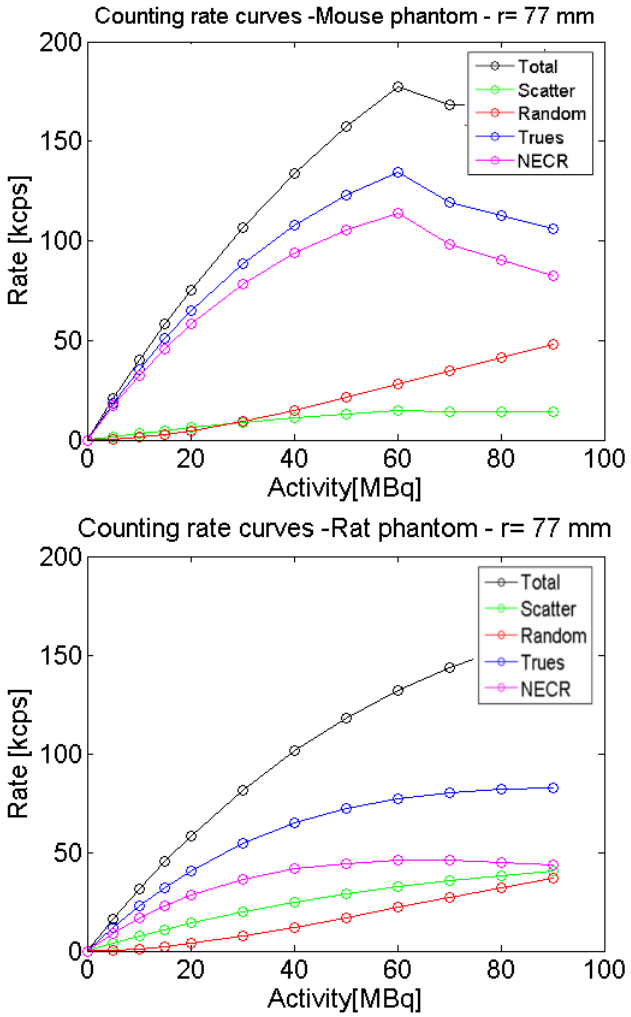

Figure 5.1: Count rate curves for **r77-miniPET**. Top: mouse phantom. Bottom: rat phantom. The peak NECR is achieved at high levels of activity, 60 MBq for the mouse phantom and more than 90 MBq for the rat phantom. As expected, the true, total and noise-equivalent count rates decrease when using the rat phantom.

the count rate performances of a PET device. In this work, the effect of deadtime was a head scratcher; even if the results presented in the previous paragraph are obtained by setting the deadtime to 200 ns (realistic value obtained from a real machine that used the same crystals [1]), the very first simulations had been run with a deadtime of 3 μs, and the results then obtained were way different from the

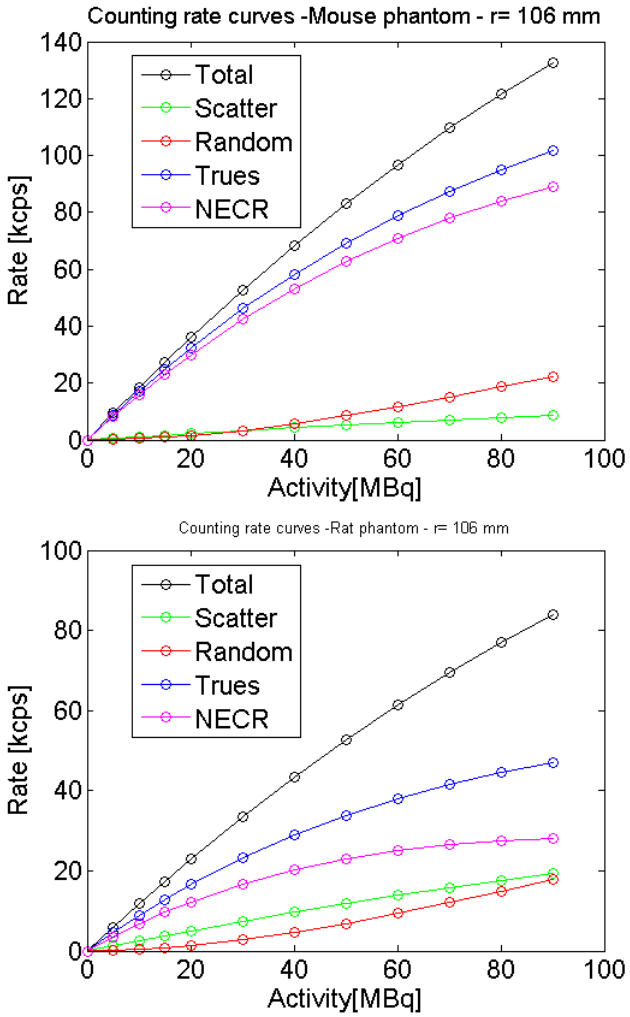

Figure 5.2: Count rate curves for **r106-miniPET**. Top: mouse phantom. Bottom: rat phantom. The count rate performances are worse than **r77-miniPET** in terms of peak NECR; however, the peak activity is higher.

ones here presented. In order to explore the effects of this parameter on count rate, other simulations were made after setting up the deadtime to 1 μs. Figure 5.3 shows a comparison of NECR curves, obtained from the same camera but with different deadtime values: decreasing the deadtime moves the peak in the count rate to higher activity levels; moreover, the count rate itself reaches considerably higher levels. This behavior is brought to extreme when the deadtime of the detector is completely

	r77		r106	
	mouse	rat	mouse	rat
peak NECR [kcps]	114	46	89	28
peak activity(NECR) [Mbq]	60	60	>90	>90
peak trues [kcps]	134.418	82.493	101.588	46.878
peak activity(trues) [Mbq]	60	90	>90	>90
SF [%]	8.00	22.4	6.00	22.2

Table 5.1: Table summarizing peak values and Scatter Fraction (SF) of the two different geometries tested

removed (data not shown). This fact is of great interest, especially because the fraction of scatter coincidences doesn't increase at the same pace. Hence, it is confirmed that higher count rate performances can be reached if the deadtime in the detection elements is reduced.

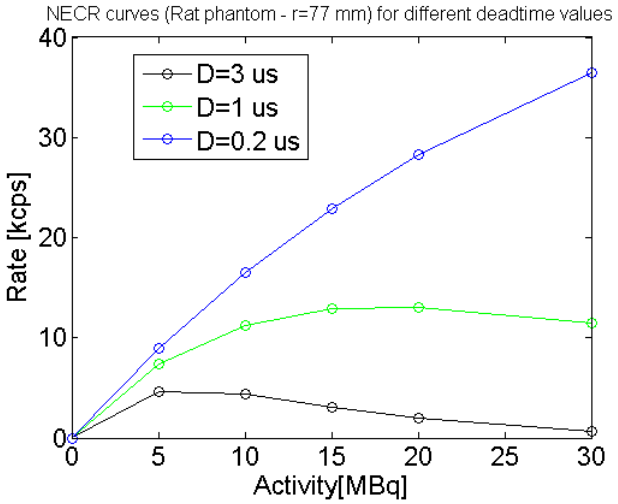

Figure 5.3: Effect of deadtime on count rate performances. The overall behaviour of the curves is similar: in all cases NECR increases, reaches a peak and eventually starts decreasing. However, the lower the deadtime, the higher the peak NECR and the activity at which it is reached.

Sensitivity

The results obtained from sensitivity tests are summed up in figure 5.4 and in table 5.2: the maximum value of sensitivity is reached at the center of the camera, as

expected, and the value obtained with **r77-miniPET** is similar to the one obtained with the miniPET II design (10 vs 12.3 cps/kBq, respectively); the simulations using r=106, on the other hand, show a sensitivity that is almost half of the r77 value: this is consistent with the fact that the gaps between the detectors determine higher count losses' rates, and it definitely speaks in favour of r77 design.

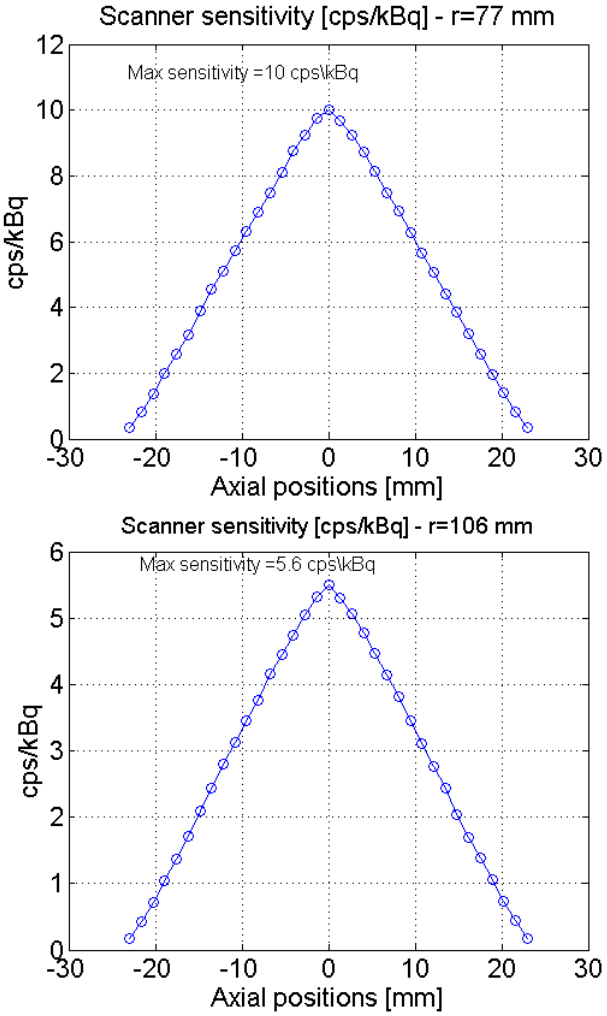

Figure 5.4: Axial sensitivity profile. Top: **r77-miniPET**. Bottom: **r106-miniPET**. In both cases the maximum count rate is achieved at the center of the camera and goes down to zero at the edges of the axial FOV. However, the peak value is higher in **r77-miniPET** design.

	r=77 (10 det)	r=106 (10 det)	r=106 (12 det)
peak value [cps/kBq]	10	5.6	6.3
variation(0-25 mm)	-15%	-31%	not available

Table 5.2: Peak values and radial variation of sensitivity.

As described in Figure 5.5 and in table 5.5, the r77 camera behaves better when it comes to test radial sensitivity, too.

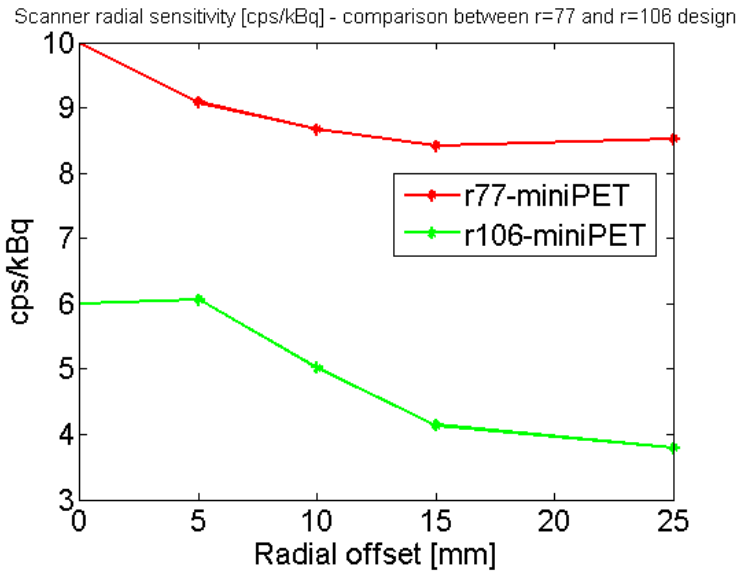

Figure 5.5: Radial sensitivity: comparison between **r77-miniPET** and **r106-miniPET**. The loss in sensitivity throughout the radial FOV is bigger if considering r106 design: -31% vs -15% obtained if using **r77-miniPET**

Spatial resolution

The results obtained from simulations of spatial resolution for **r77-miniPET** are summarized on Figure 5.7, 5.8 and in table 5.3. It is interesting to notice that, along x (*radial*) direction, the values show a trend that is opposite to the one expected, since FWHM is high at the center of the camera and decreases if the source is moved away from it. This effect is not present along y (*tangential*) direction. It has been proved that this effect is due to the geometry of the camera (see Figure 5.6): rotating the gantry by 90 degrees, acquiring again images of the source and applying to these new images the same algorithm as before, produces a FWHM(x)=1.54 mm

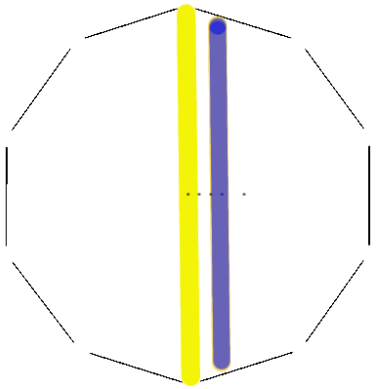

Figure 5.6: Sketch of the geometry and spatial resolution issues: if the source is positioned at the center of the camera, some LOR are lost due to the spacing between the detectors and, among those that are recorded, some of them don't pass exactly through the center, thus deteriorating spatial resolution. This effect is lower if the source is moved away from the center (blue line), since the area is almost always covered by detection elements (even rotating the camera).

and a FWHM(y)=2.04mm, which is almost exactly the opposite as before. The reconstruction software of the real machine will have to take into consideration this effect and apply the necessary corrections. Bearing this in mind, the behaviour of the machine in terms of spatial resolution is satisfying and encouraging. Despite poor sensitivity, results of spatial resolution tests are pretty encouraging even for **r106-miniPET** (Figure 5.9 and 5.10, table 5.4)

Offset[mm]	FWHM X	FWHM Y	FWHM Z	FWTM X	FWTM Y	FWTM Z
0	2.03	1.59	1.50	3.00	2.75	2.70
5	2.01	1.86	1.70	3.00	2.92	2.81
10	1.76	1.89	2.42	2.85	2.92	3.25
15	1.50	2.19	2.79	2.69	3.11	3.59
25	2.58	2.59	3.01	3.65	3.35	3.98
At 1/4 of axial FOV from center						
Offset[mm]	FWHM X	FWHM Y	FWHM Z	FWTM X	FWTM Y	FWTM Z
0	2.04	1.57	1.49	3.01	2.73	2.65
5	2.05	1.81	1.59	3.02	2.88	2.67
10	1.81	1.85	2.08	2.88	2.9	2.96
15	1.58	1.89	2.31	2.74	2.93	3.24
25	2.96	2.21	2.86	4.17	3.13	3.83

Table 5.3: Resolution for r77 camera. All values in [mm].

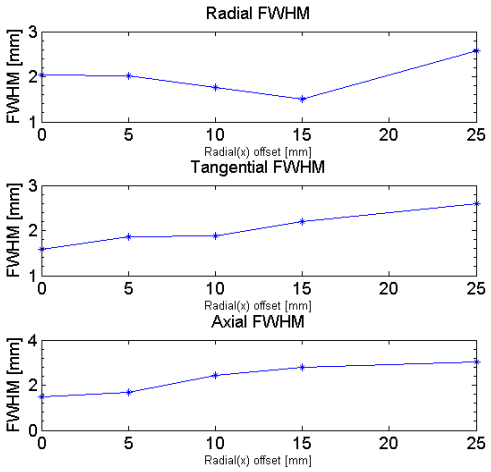

Figure 5.7: Spatial resolution across the radial FOV for **r77-miniPET**. FHWM values with no axial offset. FWHM never reaches values lower than 1.50 mm, and the minimum FWTM is reached at 15mm offset with 2.69 mm. The effect of non orthogonal axes of symmetry of the 10-detectors geometry is evident along x-direction.

Image quality

The data collected from image quality tests —see figure 4.6 on page 44 for the details of the *Derenzo phantom*— were backprojected and the results obtained (central slice only) are shown in Figure 5.11: speaking about **r77-miniPET**, it is clear that the bigger rods (up to 2.4mm) are almost completely resolved; it is almost impossible to discriminate between the cylinders whose diameter is 1.2mm, while the ones with d=1.6 can be distinguished, but the quality is still too poor to provide a good image. A different reconstruction algorithm could possibly help to improve SNR, remove artifacts and produce better images (see Chapter 2). As for **r106-miniPET**, the same amount of time leads to the collection of fewer coincidences, reducing image quality even further (Figure 5.11, right).

These results are encouraging, especially if considered that the crystals are simple (no DOI corrections are applied) and the FBP reconstruction algorithm that has been used is one of the simplest available.

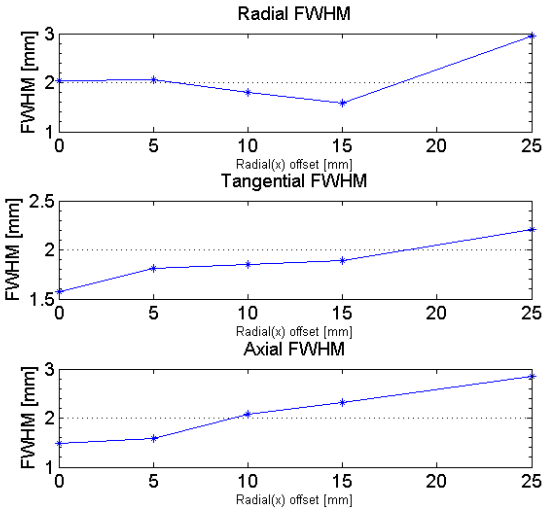

Figure 5.8: Spatial resolution across the radial FOV, FWHM values, for **r77-miniPET**. FWHM values at 1/4 of axial FOV (-11.81 mm from center along z direction).

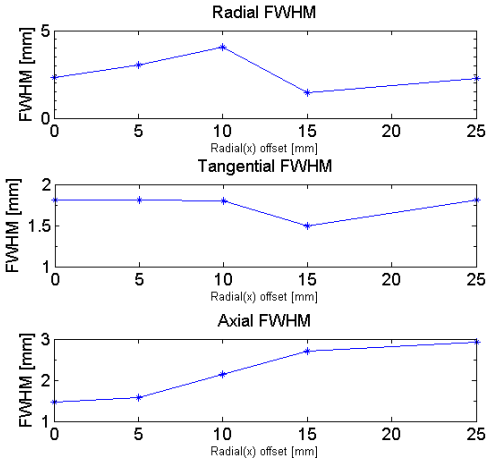

Figure 5.9: Spatial resolution across the radial FOV for **r106-miniPET**. FHWM values with no axial offset.

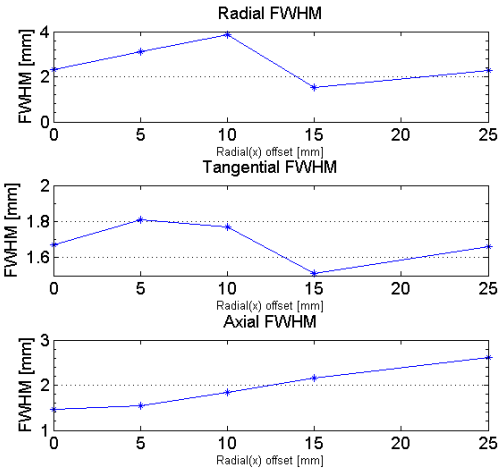

Figure 5.10: Spatial resolution across the radial FOV for **r106-miniPET**.FWHM values at 1/4 of axial FOV (-11.81 mm from center along z direction)

Offset[mm]	FWHM X	FWHM Y	FWHM Z	FWTM X	FWTM Y	FWTM Z
0	2.30	1.81	1.46	3.16	2.89	2.62
5	3.05	1.81	1.57	4.05	2.88	2.73
10	4.06	1.8	2.15	5.32	2.88	3.08
15	1.43	1.49	2.7	2.58	2.66	3.4
25	2.27	1.81	2.92	3.16	2.89	3.82
At 1/4 of axial FOV from center						
Offset[mm]	FWHM X	FWHM Y	FWHM Z	FWTM X	FWTM Y	FWTM Z
0	2.32	1.67	1.46	3.2	2.81	2.62
5	3.12	1.81	1.54	4.19	2.88	2.66
10	3.86	1.77	1.84	5.21	2.85	2.81
15	1.53	1.51	2.16	2.71	2.7	3.06
25	2.28	1.66	2.62	3.17	2.79	3.59

Table 5.4: Resolution for r106 camera. All values in [mm].

5.2 Discussion and comparison with other small-animal cameras

Small animal PET cameras have started to be developed in the last decade, when the need of new devices able to image smaller and smaller structures has become impelling, both in medical practice (especially in onchology) and in the research

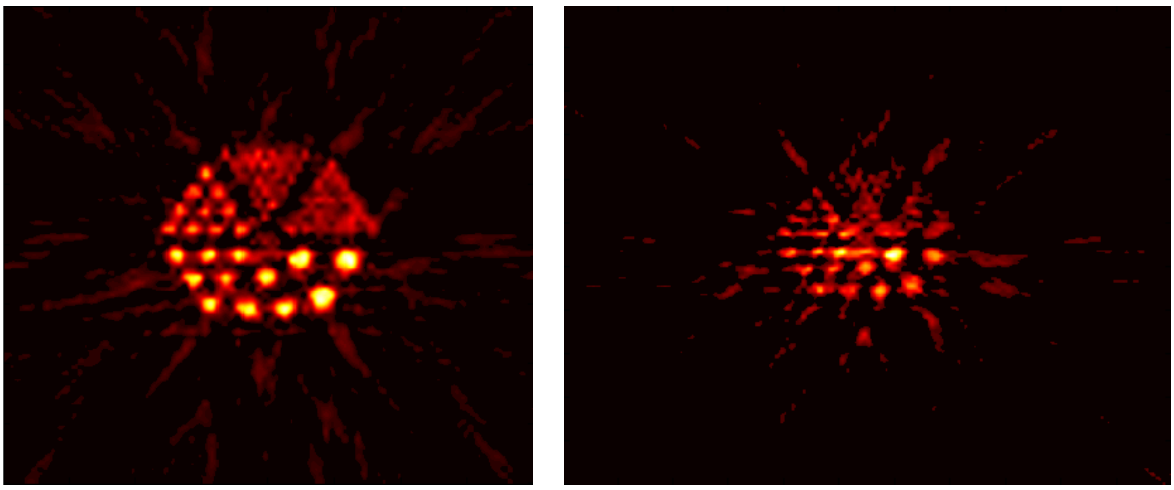

Figure 5.11: Reconstructed Derenzo phantom(see figure 4.6 on page 44 for details). Left: **r77-miniPET**; right: **r106-miniPET**. **r77-miniPET** produces better images, but it has to be considered that acquisition times were the same for both geometries. This implies that, in **r106-miniPET**, less coincidences have been collected for reconstruction.

field. It is interesting to compare the performances of **r77-miniPET** in comparison with other scanner designs, in order to understand which are the most important parameters that influence the results obtained. Some comparative studies have already been performed [9]; the scanner chosen here are miniPET II, because it is the immediate predecessor of the camera simulated in this work, 3 models of commercial devices (clearPET [27], miniPET Focus 120 [32] and GE Healthcare eXplore VISTA [33]), because this is the state-of-the-art in today clinical practice, and two new devices (nanoPET/CT [9] and YAP-(S)PET [34]), the former because it is one of the latest achievements in the field of small-animal imaging so far, the latter just to have a comparison with a camera with completely different design and still pretty good performances.

The main technical specifications of the devices here compared are presented on table 5.2, together with the main results obtained from testing them. Most of the data presented come from tests performed folllowing NEMA recommendations, and this fact makes it easier to compare the results obtained with the different geometries. Nevertheless, there are still some parameters that can be freely set (i.e. coincidence window, energy window) and some hardware details not explicitly declared (i.e. electronics used, deadtime, speed and size of processing hardware, i.e. RAM modules [1]). All these factors can deeply affect the results obtained or lead to wrong conclusions, so each comparative has to be carefully weighted in this

Scanner	**r77-miniPET**	**r106-miniPET**	miniPET II (2009)	ClearPET (2007)*	**Focus 120 (2007)**	VISTA (2006)	nanoPET/CT (2011)	YAP-(S)PET (2007)
Full ring(F) or Modular (M)	M	M	M	M	M	M	M	M
Number of detectors	10	10	12	20	96	36 (2 rings of 18)	12	4
Total number of crystals (tnc)	12250	12250	14700	10240 (5120x2 layers)	13824	12168 (6084x2 layers)	37908	1600
Number of crystals/detector (nc)	1225 (35x35)	1225 (35x35)	1225 (35x35)	64x2 (8x8, 2 slices)	144 (12x12)	169 (13x13)	3159 (39x81)	400 (20x20)
Crystal Type	Single-layer crystal	Single-layer crystal	Single-layer crystal	Dual-layer crystal (front layer: LYSO; back layer: LuYAP)	Single-layer crystal	Dual-layer phoswich (front layer: LYSO; back layer: GSO)	Single-layer crystal	Single-layer crystal
Crystal size [mm]	1.27x1.27x12	1.27x1.27x12	1.27x1.27x12	2x2x10 for LYSO and LuYAP (total length: 20 mm)	1.5x1.5x10	1.45x1.45x7 for LYSO and 1.45x1.45x8 for GSO (total length: 15 mm)	1.12x1.12x13	2x2x25
Crystal pitch (pc) [mm]	1.35	1.35	1.35	2.3	1.59	1.55	1.17	n.a.
Crystal material	LYSO	LYSO	LYSO	LYSO-LuYAP	LSO	LYSO:Ce + GSO	LYSO:Ce	YAP:Ce
Module packing fraction [%]	88	88	88	92	89	87	92	n.a.
Axial FOV [mm]	50	50	50	110	76	48	94.8	40
Ring diameter (radial FOV) [mm]	154	212	212	135	150	118	181	150
Solid angle coverage	**0.27**	0.14	0.17	0.36	**0.44**	0.29	0.47	0.09 [a]
Energy window [keV]	350-650	350-650	350-650	250-750	250-750	250-700	250-750	50-850
Coincidence window [ns]	**3**	3	3	12	**6**	6.5	5	
Fit	Parabolic	Parabolic	Parabolic	Parabolic	n.a.	n.a.	n.a.	
Reconstruction method	SSRB+2D FBP	SSRB+2D FBP	SSRB+2D FBP	3D FBP	FORE+FBP	FORE+FBP	SSRB+2D FBP	FBP
Scatter fraction (mouse phantom) [%]	8	6	12.3	31	15.9	26.6	15	21.7
Peak NECR [kcps]	**114.107**	89.195	55.1	73.4	**869**	126.8	430	30
Activity of peak NECR [Mbq]	**60**	90	38.9	27 ***	**160.8**	23 ***	36	20
Absolute sensitivity[%]	5.73	3.129	3 ****	4.7	7 (3.8 if e.w.=[350-650])	4	7.7(4.67 if e.w.=[350-650])	2.3
Spatial resolution (CFOV) [mm]								
Axial	1.50	1.46	1.4	3.1	1.44	1.75	1.4	2
Radial	**1.59**	1.81**	1.4	1.4	**1.18**	1.75	1.2	2.4
Spatial resolution (25 mm from CFOV) [mm]								
Axial	3.01	2.92	2.3	3.2	2.1	2.1	2.1	n. a.
Radial	2.59	1.81**	2.3	1.5	2.45	2.1	2.4	n. a.

[a] * full ring, small diameter (the scanner has other modalities)
** correction for geometry have to be applied
*** Calculated assuming line source of r=15mm and h=70mm
**** Data differ from reference paper [1]

Packing fraction [%]=$\frac{nc * sc^2}{nc * pc^2}$; Solid angle coverage=$\frac{tnc * sc^2}{4\pi r^2}$. sc=crystal front side.

light. Moreover, all data included in the table come from real cameras and real acquisitions, so the results obtained with our simulations of **r77-miniPET** and **r106-miniPET** could be slightly different from real output [1]. ***In the table, data coming from simulated cameras are separated with a vertical line from the ones obtained from real cameras.***

The comparison of the results got with our 10-detector design with other geometries is interesting and instructive. First of all, it has to be noted that all the cameras here presented are based on a modular geometry: this means that ideally it should be possible to move the detectors and adapt them to different phantom or object sizes. Moreover, modularity implies more flexibility and leaves room for possible improvements in design (this is actually the case of miniPET II). Secondly, the number of detecting elements has to be considered: **r77-miniPET** (together with **r106-miniPET**) has the lowest number of crystals after clearPET; this is of great importance when it comes to consider the price-to-benefits ratio, since a high number of detectors generally implies higher costs. In terms of crystal arrangement within the crystal, different solutions can be considered: square matrices of crystals are the most common solution, but putting more crystals along, i.e., the axial direction can increase axial FOV avoiding the gaps between adjacent rings (it happens in clearPET, and problems in detecting coincident events are documented [27]); this problem is not of crucial importance and it can be easily got around by, for example, moving the bed and performing multiple acquisitions, but at the price of longer acquisition times.

As for the tested performances, as said before, most of these cameras have been evaluated following NEMA recommendations.
In terms of **scatter fraction**, **r77-miniPET** is one of those that expected to behave better, achieving a good 8%. The camera will have less noise in the final image, but it has to be remembered that this value is strongly dependent on the lower energy threshold applied, so this can bias the comparison with the other commercial cameras (whose energy window was set to 250-750 keV). However, if compared with the result obtained with miniPET II, the results got with **r77-miniPET** are encouraging and speak in favour of 10-detectors design. Count rate performances improve too, if compared with miniPET II, since the peak count rate is achieved at higher levels of activity and the peak itself is more than doubled (114 kcps vs 55 kcps). This means that the camera will be able to image objects at lower activity levels, without degradations due to scatter events. Since some of the tests performed on small animals (e.g. glucose utilization, or bone and heart metabolism [35])require activity levels lower than 50 MBq , the ability to reach high count rates at low activity levels is the most desirable outcome: with these regards,

[1] Many studies have been performed in order to validate GATE simulations of SPECT, PET and small-animal PET against real data, see for example [23] and [33]. GATE simulations are a reliable tool in molecular imaging, and the results coming from simulations using this software follow the real trend with only small variations.

r77-miniPET shows a behavior that is better than miniPET II. **r106-miniPET** well behaves aswell, achieving good scatter fraction values (which make sense, since the solid angle coverage is lower) and realtively high peaks of activity; the count rate obtained is coherently lower, but still it achieves values higher than miniPET II. Even if these results are encouraging if compared with 12-detectors design, they are far from the values obtained using other commercial cameras. Considering NECR preformances, for example, Focus 120 achieves astonishing results, with a peak value of 869 kcps at 160 MBq that can be partially explained by considering the different energy window and the different geometric efficiency (mainly due to the bigger axial FOV).

Speaking about mean absolute **sensitivity**, both **r77-miniPET** and **r106-miniPET** here simulated show values that are very encouraging, even if they are lower if compared to many of the other commercial devices here taken as comparison. In some cases, however, the high values reached by the competitors can be explained by the extended axial FOV or solid angle coverage(this is the case of clearPET, Focus 120 and nanoPET), together with the different coincidence window and energy window parameters. In any case, the result of **r77-miniPET** is in good agreement with the geometric efficiency of the scanner (in turn related with the solid angle covered by the detection elements), and it's (coherently) higher than what was obtained with miniPET II.

Finally, interesting results come from the comparison of **spatial resolution** values: first of all, it can be noted that not always thinner crystals mean better performances (cfr. spatial resolution of Focus 120 vs miniPET II). **r77-miniPET** achieves a good 1.54mm FWHM in the center of the camera, along x and y direction (assuming corrections for geometry have been applied), which is only 10% higher than the value got from miniPET II. It deteriorates along the radial FOV of 59% with respect to its initial value, but this behavior is natural and it is due to increased parallax effect. Only two cameras keep their FWHM value uniform throughout the radial FOV, clearPET and VISTA. They actually are the only two scanners that apply one of the possible methods for parallax error correction (dual layer crystals with different scintillation times); among those that don't apply any correction, **r77-miniPET** is the one that behaves better in the x-y plane. Looking at axial resolution, on the contrary, the loss in performance with **r77-miniPET** is substantial (FWHM value doubled with respect to axial fresolution at CFOV) and can be partially attributed to the simple rebinning method applied. Regarding spatial resolution, one last point that has to be emphasized: the reconstruction algorithm plays an important role in determining FWHM and FWTM values, and can greatly contribute to improve image quality. All the results presented here are uniform and comparable, since they all come from Filtered Backprojection with no smoothing (as NEMA suggests). However, the results in term of spatial resolution ad image quality could improve if using other reconstruction techniques, such as OSEM or MLEM, instead of FBP ([35], [36] and [27]). Therefore, it could be pos-

sible to image objects with more precision only by working on the post-processing phase of the test. As a conclusion of this section on comparison of performances,

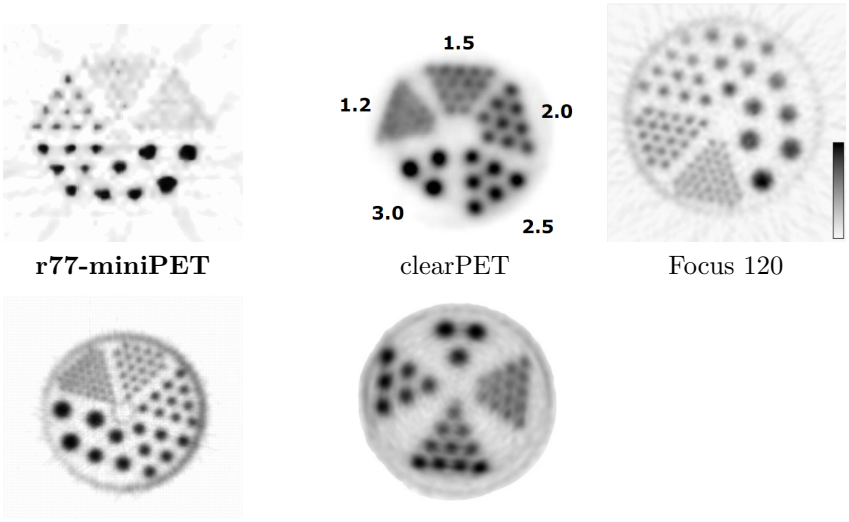

Figure 5.12: Reconstructed images (FBP) of Derenzo phantom. **r77-miniPET**, VISTA and Focus 120 use the same Derenzo phantom (see figure 4.6 on page 44). YAP-(S)PET uses a phantom where the diameters of the rods are 3.0, 2.5, 2.0, and 1.5 mm. The values for the rods of the phantom used in clearPET are indicated in the figure itself.

figure 5.12 shows a comparison of the Derenzo phantoms, obtained with some of the cameras here analyzed: even visually, it can be noted that **r77-miniPET** is able to portray with accuracy rods up to 1.6mm diameter, and its overall performances seem comparable with its commercial rivals.

Finally, the comparison with YAP-(S)PET was introduced to show that it's not said that high number of detection elements is synonymous with good performances. YAP-(S)PET is made up of 4 detectors but, thanks to fast readout electronics, and probably to some other implementative details, it is able to achieve good results, especially if compared with the very low solid angle coverage. Unfortunately, the details given for this camera are quite few, but it would be interesting to know which are the main differences in order to design a device that best puts together low cost and more than decent performances.

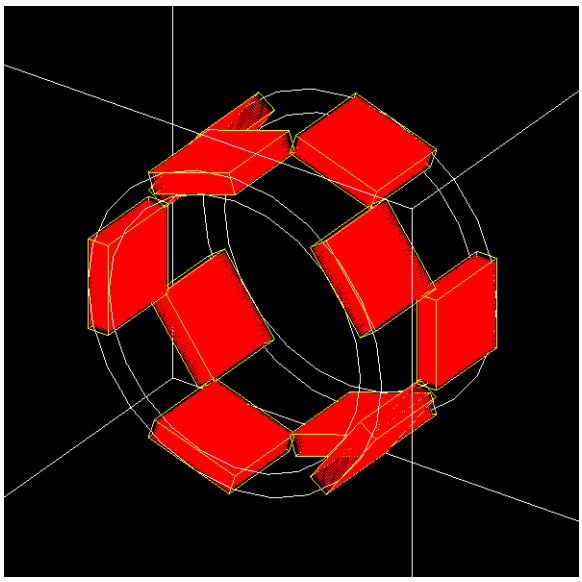

Figure 5.13: 10 detectors arranged into 2 parallel rings: r77-PENTA

First tests with two other detector arrangements

From these simulations, all things considered, it looks like the results of **r77-miniPET** are encouraging: the removal of two detectors from miniPET II shouldn't affect too much the performances of the camera, while keeping the costs even lower. However, it has been demostrated that changing the Axial FOV (AFOV) can influence the performances of the scanner in terms of scatter fraction, NECR, sensitivity and spatial resolution [37]. Hence, we tried to keep the ring diameter constant at d=154 mm, but the 10 detectors were arranged in two rows of 5 detectors each, shifted one another so that a detector in the second row covered the gap between two detectors in the first row. A sketch of the new geometry, referred to as ***r77-PENTA*** from here on, is presented in Figure 5.13.
Another attempt was made by removing two more detectors from **r77-miniPET** (total number of detectors= 8), arranging them in a single row and reducing the radial FOV to 120 mm (effective FOV 85 mm, which is barely sufficient to image an average rat). The resulting camera (***r60-miniPET***) is shown on Figure 5.14. The solid angle coverage in this case increases up to 0.44, which should produce a high sensitivity but, in turn, higher scatter fraction. The removal of two detectors was done because the 10 detectors geometry doesn't show the same symmetry with respect to any orthogonal axes taken, so possible artifacts could occur in the image reconstruction phase, which could in turn affect spatial resolution results (Figure 5.6).

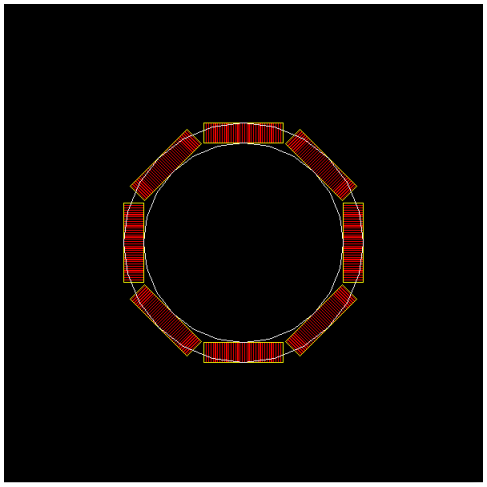

Figure 5.14: 8 detectors arrangement: r60-miniPET.

A selection of tests was applied to the novel geometries: attention was focused on those tests that looked more meaningful to understand the overall performances of the scanners. A summary of the tests taken is given below:

- sensitivity and spatial resolution:
  1) No radial(x) offset and no axial(z) offset: $(r_{off} = 0mm, a_{off} = 0mm)$
  2) 15 mm radial(x) offset and no axial(z) offset:$(r_{off} = 15mm, a_{off} = 0mm)$
  3) No radial(x) offset and -17.5 mm axial(z) offset:$(r_{off} = 0mm, a_{off} = -17.5mm)$
  4) 15 mm radial(x) offset and no axial(z) offset:$(r_{off} = 15mm, a_{off} = -17.5mm)$

- scatter fraction at 5MBq activity

- NECR value at 5MBq activity

The same tests were performed both on **r77-PENTA** and on **r60-miniPET**. The only difference was that, in **r60-miniPET**, the axial offset was set to $a_{off} = -11.81$ mm (instead of -17.5mm).

	FWHM (transaxial) [mm]	FWTM (transaxial) [mm]	FWHM (axial) [mm]	FWTM (axial) [mm]	sensitivity [cps/kBq]
$a_{off} = 0mm, r_{off} = 0mm$	1.51	2.70	1.89	2.93	8.58
$a_{off} = 0mm, r_{off} = 15mm$	2.02	2.99	3.66	5.04	4.97
$a_{off} = -17.5mm, r_{off} = 0mm$	1.48	2.69	2.40	3.24	2.55
$a_{off} = -17.5mm, r_{off} = 15mm$	1.40	2.56	2.30	3.21	2.68
scatter fraction (mouse phantom)		7.6%			
NECR at activity=5MBq		15	kcps/MBq		

Table 5.5: Table summarizing values obtained from simulations of **r77-PENTA** at specific, most meaningful positions (assuming corrections for geometry applied)

	FWHM (transaxial) [mm]	FWTM (transaxial) [mm]	FWHM (axial) [mm]	FWTM (axial) [mm]	sensitivity [cps/kBq]
$a_{off} = 0mm, r_{off} = 0mm$	1.46	2.62	1.57	2.73	12
$a_{off} = 0mm, r_{off} = 15mm$	1.95	2.95	2.77	3.56	10.43
$a_{off} = -11.81mm, r_{off} = 0mm$	1.53	2.70	1.56	2.71	6.6
$a_{off} = -11.81mm, r_{off} = 15mm$	1.62	2.68	2.47	3.42	6.2
scatter fraction (mouse phantom)		9%			
NECR at activity=5MBq		20	kcps/MBq		

Table 5.6: Table summarizing values obtained from simulations of **r60-miniPET** at specific, most meaningful positions

r77-PENTA

Table 5.5 shows the results obtained from these simulations. If scatter fraction is considered, at low activity levels it stays similar to the value obtained from **r77-miniPET**(7.6% vs 8%, respectively); moreover, spatial resolution of a point source positioned in the middle of the camera is as good as 1.60 mm FWHM along x direction, which is even lower along y direction. This fact can be attributed, again, to the asymmetry of the geometry. Axial resolution is slightly worse than **r77-miniPET** aswell. As for sensitivity, the peak count rate at the center of the camera is lower (8.58 cps/kBq), but still quite good, especially if compared with the performances of **r106-miniPET**. Other tests were done by moving the source away from the center, at -17.5 mm along z direction and at 15 mm offset alog x direction. In the first case ($r_{off} = 0, a_{off} = -17.5mm$) , sensitivity fastly decreases to 2.55 cps/kBq, while spatial resolution stays low both in x and y direction (1.48 mm FWHM). Along z direction the value is still high (2.40 mm FWHM). Considering, on the other hand, the results obtained with the source shifted radially($r_{off} = 15mm, a_{off} = 0mm$) , resolution in the transaxial direction is still pretty good (better than **r77-miniPET**, with 2.02 mm FWHM), while the problem along the axial direction is still well present (3.66 mm FWHM). Sensitivity reaches almost half of its initial value (4.97 cps/kBq), and this would lead to prefer the geometry of r77 and r106 miniPET, since the radial loss of sensitivity is much lower — especially with **r77-miniPET**. Similar results occur when the source is shifted both radially and axially ($r_{off} = 15mm, a_{off} = -17.5mm$): sensitivity and spatial resolution worsen, thus making this type of geometry uneffective for small-animal PET imaging.

From these first tries, the idea of arranging the same number of detectors into two rows seems uneffective: it doesn't introduce any improvements in terms of spatial resolution, uniformity of sensitivity or axial resolution. On the contrary this geometry, characterized by wide gaps between detection modules, produces a non-uniform sampling of the FOV, thus being uneffective to image all areas equally well. All things considered, better results are obtained with all ten detectors in a single row.

r60-miniPET

The first data obtained with the 8-detectors arrangement look even more encouraging than **r77-miniPET** (Table 5.6). With a source positioned at the center of the camera, sensitivity reaches a peak of 12 cps/kBq, while spatial resolution in the transaxial FOV is even better than **r77-miniPET** (1.46 mm FWHM in the transaxial plane, 1.57mm FWHM along z direction). Moreover, these results confirm that the octagonal geometry, like the dodecagonal one, is free from the artifacts produced when using 10 detectors (figure 5.6).

Moving the source radially ($r_{off} = 15mm$) doesn't affect too much the performances in terms of sensitivity, since the value obtained is 10.43 cps/kBq: the loss throughout the radial FOV is then lower (-12%) than the one obtained with r77 (-15%). This fact is encouraging since it means that the count rate is more uniform for all the points in the FOV of the camera. The performances of spatial resolution in the transaxial plane, however, are slightly worse than those from **r77-miniPET**. If the source is moved along z-axis ($a_{off} = -11.81mm, r_{off} = 0mm$), spatial resolution stays low, while sensitivity almost halves its initial value (6.6 cps/kBq): this behaviour is natural and similar to the one of **r77-miniPET**. Finally, moving the source both axially and radially, doesn't seem to affect performances in terms of transaxial spatial resolution, whereas axial resolution is slightly worse than the one obtained with **r77-miniPET** (2.47 mm FWHM vs 2.31 mm FWHM). Table 5.6 summarizes the results obtained.

Chapter 6

Conclusions

In the present work, expected performances of a 10-detectors PET device for small-animal imaging have been tested, according to National Electrical Manufacturers Association (NEMA) requirements. The results are encouraging, especially if compared to this camera's immediate predecessor (miniPET II): count rate is higher and the peak is reached at higher values; spatial resolution is only 10% worse, while scatter fraction is 4% lower. The number of crystal elements is low, especially if compared with most clinical PET now used in everyday practice, and the costs should be kept low if considering that simple LYSO, single-layer crystals have been simulated. All things considered, the 10-detectors design works well, and the idea of removing two detectors from miniPET II is possible with no dramatic loss of performances.

Compared to other PET devices, **r77-miniPET** doesn't have exceptional count rates, neither achieves perfect image quality, but it is a good starting point for designing a device which is well-performing and relatively low cost at the same time. Moreover, including a CT module could increase even further the quality of the images obtained. In fact, it could allow to match the good description of radiotracer distribution, obtained with **r77-miniPET**, with a more detailed anatomical description of the area under examination.

The idea of further decreasing the number of detector modules was considered, and actually good results were obtained from some simple, preliminary trials performed with 8 detector modules in a ring. Going down even further with the number of detector blocks (i.e. 7 or lower) is feasible, but different components (crystals, electronics, ...) should be used in that case. In fact, the effect of parallax phenomenon would become non-negligible and could have increasing influence on spatial resolution, especially if no corrections for that were applied. All things considered, and looking at the goal miniPET was aiming to, these results don't speak in favour of the 12-detectors design, but instead suggest the removal of two detectors from this camera. 10 detectors could then make up a camera with low costs and decent performances. Further studies should be made in order to assess

the properties —and/or the possible superiority— of the 8-detectors arrangement.

Bibliography

[1] S. A. Kis, I. Lajtos, M. Emri, L. Tron, G. Opposits, T. Bükki, G. Hegyesi, J. Imrek, I. Valastyán, J.Molnár, D. Novák, and L. Balkay, "Performance Test of the MiniPET-II Small Animal Scanner According to the NEMA NU-4 Standard," *IEEE Nuclear Science Symposium Conference Record*, vol. 1-5, pp. 3185–3189, 2009.

[2] N. E. Bolus, R. George, J. Washington, and B. R. Newcomer, "PET/MRI: The Blended-Modality Choice of the Future?," *Journal of Nuclear Medicine and Technology*, vol. 37, pp. 63–71, 2009.

[3] `http://depts.washington.edu/nucmed/IRL/pet_intro`, 1999.

[4] H. Jadvar and J. A. Parker, *Clinical PET And PET/CT*. Springer, 2005.

[5] "NEMA Standards Publication NU 4-2008 Performance Measurements of Small Animal Positron Emission Tomographs,."

[6] W. W. Moses, "Fundamental limits of spatial resolution in PET," *Nuclear Instruments and Methods in Physics Research Section A: Accelerators, Spectrometers, Detectors and Associated Equipment*, vol. 648, Supplement 1, p. S236:S240, 2010.

[7] C. S. Levin and E. J. Hoffman, "Calculation of positron range and its effect on the fundamental limit of positron emission tomography system spatial resolution," *Phys. Med. Biol.*, vol. 44, p. 781:799, 1998.

[8] J. L. Humm, A. Rosenfeld, and A. Guerra, "From PET detectors to PET scanners," *European Journal of Nuclear Medicine and Molecular Imaging*, vol. 30 (11), pp. 1574–1597, 2003.

[9] I. Szanda, J. Mackewn, G. Patay, P. Major, K. Sunassee, G. E. Mullen, G. Nemeth, Y. Haemisch, and P. J. B. andPaul K. Marsden, "National Electrical Manufacturers Association NU-4 Performance Evaluation of the PET Component of the NanoPET/CT Preclinical PET/CT Scanner," *Journal of Nuclear Medicine*, vol. 52, pp. 1741–1747, 2011.

[10] S. Vallabhajosula, *Molecular Imaging: Radiopharmaceuticals for PET and SPECT*. Springer, 2009.

[11] S. Derenzo, M. Weber, E. Bourret-Courchesne, and M. Klintenberg, "The quest for the ideal inorganic scintillator," *Nuclear Instruments and Methods in Physics Research*, vol. 505, pp. 111–117, 2003.

[12] J. T. Bushberg, J. A. Seibert, E. M. J. Leidholdt, and J. M. Boone, *The essential physics of medical imaging*. Williams and Wilkins, 1994.

[13] R. A. Ramirez, W.-H. Wong, S. Kim, H. Baghaei, H. Li, Y. Wang, Y. Zhang, S. Liu, and J. Liu, "A Comparison of BGO, GSO, MLS, LGSO, LYSO and LSO Scintillation Materials for High-Spatial-Resolution Animal PET Detectors," *IEEE Nuclear Science Symposium Conference Record*, vol. -, pp. 2835–2839, 2005.

[14] A. Quon and S. S. Gambhir, "FDG-PET and Beyond: Molecular Breast Cancer Imaging," *Journal of Clinical Oncology*, vol. 23, pp. 1664–1673, 2005.

[15] A. Kadir and A. Nordberg, "Target-Speci?c PET Probes for Neurodegenerative Disorders Related to Dementia," *Journal of Nuclear Medicine*, vol. 51, pp. 1418–1430, 2010.

[16] A. C. Kak and M. Slaney, *Principles of Computerized Tomographic Imaging*. IEEE Press, 1988.

[17] M. Beister, D. Kolditz, and W. A. Kalender, "Iterative reconstruction methods in X-ray CT," *Physica Medica*, vol. 28, pp. 94–108, 2012.

[18] H. Zaidi, *Quantitative Analysis in Nuclear Medicine Imaging*. Springer ScienceþBusiness Media, 2006.

[19] P. E. Kinahan and J. G. Rogers, "Analytic 3D image reconstruction using all detected events," *IEEE Transaction on Nuclear Science*, vol. 36, pp. 964–968, 1989.

[20] W.-M. JENG and H.-H. WANG, "An Improved 3DRP PET Image Reconstruction Method with Rebinned Direct Image Estimate," *Biomed Eng Appl Basis Comm*, vol. 18, pp. 237–244, 2006.

[21] M. Defrise, P. E. Kinahan, D. W. Townsend, C. Michel, M. Sibomana, and D. F. Newport, "Exact and Approximate Rebinning Algorithms for 3-D PET Data," *IEEE Transaction on Medical Imaging*, vol. 16, pp. 145–158, 1997.

[22] I. BUVAT and I. CASTIGLIONI, "Monte Carlo simulations in SPET and PET," *THE QUARTERLY JOURNAL OF NUCLEAR MEDICINE*, vol. 46, pp. 48–61, 2002.

[23] Jan and al., "GATE: a simulation toolkit for PET and SPECT," *Phys. Med. Biol.*, vol. -, pp. 4543–4561, 2004.

[24] `http://wiki.opengatecollaboration.org`.

[25] C. M. Pepin, P. Bérard, A.-L. Perrot, C. Pépin, D. Houde, R. Lecomte, C. L. Melcher, and H. Dautet, "Properties of LYSO and Recent LSO Scintillators for Phoswich PET Detectors," *IEEE TR*, vol. 51, p. 789:795, 2004.

[26] L. Pidol, A. Kahn-Harari, B. Viana, E. Virey, B. Ferrand, P. Dorenbos, J. T. M. de Haas, and C. W. E. van Eijk, "High Efficiency of Lutetium Silicate Scintillators, Ce-Doped LPS, and LYSO Crystals," *IEEE TRANSACTIONS ON NUCLEAR SCIENCE*, vol. 51, p. 1084:1087, 2004.

[27] M. Cañadas, M.and Embid, E. Lage, M. Desco, J. Vaquero, and J. Peírez, "NEMA NU 4-2008 Performance Measurements of Two Commercial Small-Animal PET Scanners: ClearPET and rPET-1," *Nuclear Science, IEEE Transactions*, vol. 58, p. 58:65, 2011.

[28] M. E. Phelps, *Pet: Molecular Imaging and Its Biological Applications.* Springer, 2004.

[29] B. Kemp, "PET/CT Performance Evaluation Techniques and Quality Assurance."

[30] S. Kis, I. Valastyan, G. Hegyesi, J. Imrek, G. Kalinka, J.Molnar, D.Novák, J. Vegh, L. Balkay, M. Emri, G. Molnar, I. Bagamery, T. Bukki, S. Rozsa, Z. Szabó, A. Kerek, and L. Trón, "Performance Characteristics of a miniPET Scanner Dedicated to Small Animal Imaging," *2005 IEEE Nuclear Science Symposium Conference Record*, vol. 3, pp. 4 pp.– 1648, 2005.

[31] G. B. Saha, *Basics of PET Imaging. Physics, Chemistry, and Regulations.* Springer New York, 2010.

[32] J. S. Kim, J. S. Lee, K. C. Im, S. J. Kim, S.-Y. Kim, D. S. Lee, and D. H. Moon, "Performance Measurement of the microPET Focus 120 Scanner," *Journal of Nuclear Medicine*, vol. 48, pp. 1527–1535, 2007.

[33] Y. Wang, J. Seidel, B. M. Tsui, J. J. Vaquero, and M. G. Pomper, "Performance Evaluation of the GE Healthcare eXplore VISTA Dual-Ring Small-Animal PET Scanner," *Journal of Nuclear Medicine*, vol. 47, pp. 1891–1900, 2005.

[34] N. Belcari, A. del Guerra, A. Bartoli, D. Bianchi, M. Lazzarotti, L. Sensi, L. Menichetti, M. Lecchi, P. A.Erba, G. Mariani, G. U. Corsini, and P. Sgado', "Evaluation of the performance of the YAP-(S)PET scanner and its application in neuroscience," *Nuclear Instruments and Methods in Physics Research*, vol. A 571, pp. 18–21, 2006.

[35] Y. Yang, Y.-C. Tai, S. Siegel, D. F. Newport, B. Bai, Q. Li, R. M. Leahy, and S. R. Cherry, "Optimization and performance evaluation of the microPET II scanner for in vivo small-animal imaging," *Phys. Med. Biol.*, vol. 49, pp. 2527–2545, 2004.

[36] P. S. Roldan, M. Cañadas, O. Dietzel, C. Pautrot, and A. W. I. Sarasola, "Performance Evaluation of raytest ClearPET, a PET Scanner for Small and Medium Size Animals," *IEEE Nuclear Science Symposium Conference Record*, vol. -, pp. 2859–2864, 2007.

[37] R. D. Badawil, S. Kohlmyer, R. Harrison, S. Vannoy, and T. K. Lewellen, "The Effect of Camera Geometry on Singles Flux, Scatter Fraction and Trues and Randoms Sensitivity for Cylindrical 3D PET - a Simulation Study," *IEEE TRANSACI'IONS ON NUCLEAR SCIENCE*, vol. 47, pp. 1228–1232, 2000.